Articles in PresS. J Neurophysiol (May 20, 2015). doi:10.1152/jn.00628.2014

# Cell-type- and activity-dependent extracellular correlates of intracellular spiking

Costas A. Anastassiou[1,⋆,†], Rodrigo Perin[2,⋆], György Buzsáki[3], Henry Markram[2] & Christof Koch[1]

[1] Allen Institute for Brain Science, Seattle, 98103 Washington, U.S.A.

[2] Laboratory of Neural Microcircuitry, Ecole Polytechnique Fédérale Lausanne, 4002 Lausanne, Switzerland

[3] NYU Langhorne, New York University, 10016 New York, U.S.A.

[⋆] These authors contributed equally to the work.

[†] Corresponding author:

Costas A. Anastassiou,

Allen Institute for Brain Science,

551 North 34th Street # 200, Seattle, WA 98103, U.S.A.,

Tel: +1-206-548-8434, Email: costasa@alleninstitute.org

# Abstract

Despite decades of extracellular action potential (EAP) recordings monitoring brain activity, the biophysical origin and inherent variability of these signals remains enigmatic. We performed whole-cell patch recordings of excitatory and inhibitory neurons in rat somatosensory cortex slice while positioning a silicon probe in their vicinity to concurrently record intra- and extracellular voltages for spike frequencies under 20 Hz. We characterize biophysical events and properties (intracellular spiking, extracellular resistivity, temporal jitter, etc.) related to EAP-recordings at the single-neuron level in a layer-specific manner. Notably, EAP-amplitude was found to decay as the inverse of distance between the soma and the recording electrode with similar (but not identical) resistivity across layers. Furthermore, we assessed a number of EAP-features and their variability with spike activity: amplitude (but not temporal) features varied substantially (approx. 30-50% compared to mean) and non-monotonically as a function of spike frequency and spike order. Such EAP-variation only partly reflects intracellular somatic spike variability and points to the plethora of processes contributing to the EAP. Also, we show that the shape of the EAP waveform is qualitative similar to the negative of the temporal derivative to the intracellular somatic voltage - as expected from theory. Finally, we tested to what extent EAPs can impact the lowpass filtered part of extracellular recordings, the local field potential (LFP), typically associated with synaptic activity. We found that spiking of excitatory neurons can significantly impact the LFP at frequencies as low as 20 Hz. Our results question the common assertion that the LFP acts as proxy for synaptic activity.


# Introduction

Monitoring activity in the living brain *in vivo* has traditionally been performed via extracellular voltage ($V_e$) recordings through wires, wire-bundles (for example, tetrodes, Gray et al., 1995) and, more recently, high-density silicon probes (Csicsvari et al., 2003; Buzsaki, 2004; Patel et al., 2006; Du et al., 2009) used to detect action potential (spike) signals originating from transmembrane currents of neurons mediated through the conductive extracellular medium. While such $V_e$-recordings have played a pivotal role in our understanding of circuit processing and computation, many questions still remain about events and processes related to these signals. For example, how do spatiotemporal features of the extracellular action potential (EAP) waveform change as a function of distance to the recording site, spike pattern or cell type? What are the physical properties of the medium separating a neuron from an extracellular site? How do space- and time-dependent features of the EAP-signature manifest themselves in the $V_e$-recording? In the past,

it has been difficult to address such questions mainly due to methodological challenges: voltage-recordings within, across and outside neural compartments within a few tens of $\mu$m from multiple recording sites is a non-trivial task. The few pioneering studies that did so typically recorded $V_e$ from a proximal wire- (Amzica and Steriade, 2000) or wire-bundle electrode (Henze et al., 2000), limitations that largely reduced analyses to temporal aspects of spiking and EAPs.

Understanding the spatial scale of events such as EAP-initiation and -propagation across the extracellular medium is crucial towards understanding $V_e$-signals and what these represent. For example, what is the sampling volume of an extracellular electrode? In the past, various distances have been suggested ranging from a few tens to hundreds of $\mu$m (Henze et al., 2000; Gold et al., 2006; Pettersen and Einevoll, 2008; Schomburg et al., 2012). Beyond spatial sampling, $V_e$-recordings, and EAP-waveforms in particular, are highly space- and time-dependent posing significant challenges to physiologists attempting to attribute specific EAP-shapes and -features to individual neurons (so-called units), a process often referred to as *spike sorting*. One way to increase sorting-reliability is through multiple, spatially proximal, recording sites recording from the same neuron with single-neuron recorded EAP-waveforms being different (but temporally tightly coherent) across sites (Gray et al., 1995). Hitherto the origin and degree of EAP-waveform variability from a single neuron as function of experiment-, cell type- and spike history-specific parameters remains largely unknown (Hill et al., 2011). In summary, it has been hard to bridge single-neuron, single-compartment intracellular and transmembrane physiology with extracellular signals as these are typically measured *in vivo*.

Traditionally, biophysical studies of EAP-generation and -recording are separated in two groups: first, the ones characterizing the neural origin of EAPs in terms of intracellular and transmembrane conductances contributing to these signals, and second, those characterizing the physical properties of the extracellular medium that crucially impacts EAP-features. To characterize the origin of EAPs, intracellular *in vivo* recordings have been performed (Buzsáki et al., 1996; Henze et al., 2000) (using intracellular sharp electrodes) while computational modeling has played a crucial role on bridging the gap between transmembrane events and extracellular signals (Gold et al., 2006; Pettersen and Einevoll, 2008; Schomburg et al., 2012; Reimann et al., 2013; Anastassiou et al., 2013). Notably, the wide majority of computational models studying EAPs typically assume a homogeneous, purely resistive extracellular medium. Regarding characterization of the physical properties of the extracellular medium, hitherto, measurements of extracellular conductivity have been performed with various experimental setups such as metal wires (Ranck, 1963), micro-stimulation electrodes (Logothetis et al., 2007; Goto et al., 2010), glass pipettes (Histed et al., 2009), parallel plates (Deans et al., 2007), etc. While these pioneering studies have provided insights to the conductivity of the

extracellular space, very few studies have attempted to address this question using the main particle of electrogenesis in the brain, the neuron itself. The neuron as a current source for such measurements poses a unique challenge: physiologically, neural signals can vary substantially so that the current source is not as stereotyped as current injections from specialized hardware and, technically, because intracellular and extracellular stimulation and recordings need to be performed in close proximity as EAP-signals rapidly decay within a few tens of $\mu$m from the soma (Henze et al., 2000; Buzsaki, 2004). Yet, neurons give rise to inherently nonlinear, local and transient subthreshold and spike responses, and EAP-waveforms naturally follow that pattern casting EAP- and extracellular medium characterization in the absence of actual neurons problematic.

# Materials and methods

## Slice preparation and cell identification

14 to 18 days old Wistar rats were quickly decapitated according to the Swiss Welfare Act and the Swiss National Institutional Guidelines on Animal Experimentation for the ethical use of animals. The project was approved by the Swiss Cantonal Veterinary Office following its ethical review by the State Committee for Animal Experimentation. The brain was carefully removed and placed in iced artificial cerebrospinal fluid (ACSF). 300 $\mu$m thick parasagittal slices of the primary somatosensory cortex (hind limb area) were cut on a HR2 vibratome (Sigmann Elektronik, Heidelberg, Germany). Experiments were performed at room temperature (to minimize electromagnetic interference). Cells were visualized by infrared differential interference contrast video microscopy utilizing a VX55 camera (Till Photonics, Gräfelfing, Germany) mounted on an upright BX51WI microscope (Olympus, Tokyo, Japan). Care was taken to use only 'parallel' slices, *i.e.*, slices that had a cutting plane parallel to the course of the apical dendrites and the primary axonal trunk. This ensured a sufficient preservation of both the neuron's axonal and dendritic arborizations.

## Chemicals and solutions

Slices were continuously superfused with ACSF containing (in mM) 125 NaCl, 25 $NaHCO_3$, 2.5 KCl, 1.25 $NaH_2PO_4$, 2 $CaCl_2$, 1 $MgCl_2$, and 25 D-glucose, bubbled with 95% $O_2$-5% $CO_2$. The intracellular pipette solution contained (in mM) 110 K-gluconate, 10 KCl, 4 ATP-Mg, 10 phosphocreatine, 0.3 GTP, 10 N-2 hydroxyethylpiperazine-N9-2-ethanesulfonic acid (HEPES), and 13 biocytin, adjusted to a pH 7.3-7.4 with 5 M KOH. Osmolarity was adjusted to 290-300 mosm with D-mannitol (25-35 mM). The membrane potential

values given were not corrected for the liquid junction potential, which was approximately -14 mV. Some experiments were performed under 20 $\mu$M SR 95531 hydrobromide (Gabazine; TOCRIS) to block inhibition and give rise to more spiking in the slice yet we observed no impact in terms of EAP-waveform features. Thus, results presented herein are from experiments without any synaptic receptor blockers.

## Intracellular whole-cell patch clamp stimulation and recordings

Multiple somatic whole-cell stimulation and recordings (1-4 cells simultaneously) were performed with Multiclamp 700B amplifiers (Molecular Devices, Union City, CA) in the current clamp mode. The reference electrode in all experiments was positioned approximately 1 cm from the slice in the ACSF bath in order not to be affected by the extracellular stimulus. Bridge balance compensation was continuously performed during all recordings. Data acquisition was performed via an ITC-1600 board (Instrutech Co, Port Washington, NY), connected to a personal computer running a custom written routine under IgorPro (Wavemetrics, Portland, OR). Sampling rate was 10 kHz. Patch pipettes were pulled with a Flamming/Brown micropipette puller (DMZ Universal Puller, Zeitz-Instrumente GmbH, Munich, Germany) and had an initial resistance of 4-8 M$\Omega$. 3D morphological reconstruction of biocytin-labeled cells was done under an Olympus BX 51W microscope fitted with a water-immersion 60x (numerical aperture (NA) 0.9) or an oil-immersion 100x (NA 1.35) objective using Neurolucida software (MicroBrightField, Magdeburg, Germany).

## Extracellular recordings

The 4-shank, 32-site (B32) NeuroNexus (Ann Arbor, Michigan, USA) silicon probe was attached to one of the micromanipulators and moved slowly to the target. Each shank had eight recording sites (160 $\mu$m$^2$ each site, 1-3 M$\Omega$ impedance) and inter-shank distance was 200 $\mu$m. Recordings sites were staggered to provide a two-dimensional arrangement (20 $\mu$m vertical staggered separation). Before experiments, the silicon probe was inserted in a 5% tripsin solution for approximately 60-120 minutes for cleaning purposes. Upon insertion of the silicon probe into the slice a waiting period of approximately 30-45 minutes allowed for the neurons closest to the shanks to settle in position. Whole-cell patch-clamp recordings were then performed around the probe. Data were acquired using a 32-channel Plexon (Houston, Texas, USA) wideband amplifier with sampling frequency of 10 kHz and 1000-fold amplification. Distance along the tissue depth axis between soma (intracellular site) and extracellular sites along the shank was determined via z-stacks (spacing: 1 $\mu$m). Euclidean distance between soma and each shank site was then calculated based on the distance from two landmarks, the silicon probe tip and the top edge. The soma location was taken as the center of the

soma of the patched neuron in the x-y plane of the depth where the soma appeared largest

### Theory and modeling

The compartment model used in Fig. 3 was developed by Hay and colleagues (Hay et al., 2011) and we adopted it from the NEURON database. Briefly, the authors used an automated feature-based parameter search to faithfully replicate elicitation of somatic $Na^+$-spikes in response to a prolonged step current, the generation of a $Ca^{2+}$-spike at the distal apical dendrites, as well as the interaction between the two spiking zones via the backpropagating firing. For a given modeled L5b pyramidal neuron morphology the optimization-algorithm provided a set of acceptable models (and consequently a range of model parameters) that faithfully replicate the target experimental results, as well as exhibiting the experimental variability. Experimental studies have shown that numerous such combinations of ion channel densities can result in similar firing behavior. Our simulations were performed using the NEURON software package (version 7.3). To account for the extracellular recordings sites we assumed a purely resistive extracellular medium of 2.5 $\Omega$ m resistivity with the location of the extracellular sites emulating that of an actual H32 shank (confirmed via visual inspection).

Simulated extracellular activity in Fig. 7c-e was generated using 37 ms long EAP-signatures around spike initiation time (determined intracellularly) from recorded cells summed with a lognormal spike-time distribution with a coefficient of variation (COV) of 0.5 and mean-firing frequencies of 1, 8 and 30 Hz for individual cells. Simulations involving 8 cells simultaneously active (Fig. 7i-k) used mean-firing frequencies of 1, 4 and 12 Hz per cell to obtain multi unit activity (MUA) of 8, 32 and 96 Hz, respectively. Extracellular recordings from channels that did not record spiking (assessed by a flat STA response) was used to test if extracellularly recorded action potentials produced significant changes to the extracellular signals. Two-sample paired $t$-tests were performed for 30 different frequencies at 5 Hz intervals from 2 to 147 Hz and Bonferroni correction for multiple comparisons was applied to 1% significance levels.

## Results

### Intra- and extracellular action potentials

To simultaneously monitor intracellular and extracellular voltages at multiple locations around identified neurons we modified a 12-pipette experimental setup (Anastassiou et al., 2011; Perin et al., 2011) by doing away with one of the pipettes and mounting a 4-shank/32-electrode silicon probe (8 electrodes per shank

with staggered layout and inter-electrode distance of 20 $\mu$m; see Experimental Procedures) on one of the manipulators (Fig. 1). Such silicon probes have typically been used in hippocampal and neocortical recordings *in vivo* (Mizuseki et al., 2009, 2011; Mizuseki and Buzsáki, 2013). In principle, this arrangement allowed us to position the silicon probe inside the slice at various orientations, *i.e.*, horizontal or perpendicular to the somatodendritic axis of individual neurons (for example, compare Fig. 1a with 1b-d). Yet, for the majority of experiments we positioned the silicon probe parallel to the somatodendritic axis as typically done *in vivo*. Subsequently, using up to 6 pipettes, we approached neurons in close proximity to the silicon probe shanks and performed whole-cell patch clamp experiments. At the beginning of each experiment we applied a cell-characterization protocol to determine cell properties such as input resistance and capacitance (Druckmann et al., 2011). Upon completing cell-characterization, we injected 9 s intracellular dc current stimuli $I_{inj}$ in steps of varying strength, from weak ('weak stimulation' in Fig. 1) to strong ('strong stimulation' in Fig. 1), to elicit spiking at different frequencies while simultaneously recording the intracellular voltage from the somatic patch-clamp pipette (blue traces in Fig. 1) and the extracellular voltage (red traces in Fig. 1) from different locations along the silicon probe (wideband signal was recorded, no filtering was performed). We did so for different neurons and layers of rat somatosensory cortex (hindlimb area) − herein we present our findings for L23, L4 and L5 pyramidal neurons as well as basket cells. The cell type was established by combining cell-characterization findings and morphological reconstruction (Fig. 1; black lines: dendritic arbor; red lines: axon; location of the silicon probe shanks is also designated).

## Spatial scaling of EAPs

What are the physical properties of extracellular space and how are intracellular and transmembrane signals reflected and propagated in it? We calculated the spike-triggered average (STA) from spikes as measured intracellularly by aligning the intracellular action potential (AP) waveform at the time of spike $t_{spike}$ defined as the maximum of the second-order temporal derivative of $V_i$ before the characteristic positivity (Fig. 2, left column; solid blue line: mean intracellular STA; dashed blue lines: std; dashed red line: spike time). We show the results from four individual neurons (a) a L23, (b) a L4 and (c) a L5 pyramidal neuron as well as (d) a L3 basket cell. Using the intracellular spike times, we temporally aligned the EAP-waveforms recorded along the shank closest to the patch-clamped soma for the four electrodes along the left and right side of this one shank, respectively, for the four neurons (Fig. 2, a-d, left shank side: second column; right shank side: third column; black lines: mean $V_e$). The *current source density* (CSD), approximated by the negative second spatial derivative of $V_e$ along the shank (Nicholson, 1973), is plotted in color. (Location

of the cell body along the depth axis is indicated by a triangle.) The CSD represents the volume density of the net current entering or leaving the extracellular space and has been typically used to determine spatiotemporal patterns of synaptic activity (Buzsáki et al., 2012). Our measurements show the EAP- and CSD-contribution of spiking currents of individual neurons.

A frequently made assumption is that the extracellular milieu is described by a purely homogeneous and isotropic ohmic conductivity ((Ranck, 1963; Logothetis et al., 2007; Anastassiou et al., 2011), but see also (Gabriel et al., 1996; Bédard et al., 2004)), with $V_e$ governed by Laplace's equation $\nabla^2 V_e = 0$. The boundary condition along a cable-like source is given by $(1/\rho)\nabla V_e \cdot \mathbf{n} = J$ with $J$ being the transmembrane current density and $\rho$ the extracellular resistivity (Holt, 1998). In the special case for a single point source in an unbounded isotropic volume conductor, the solution becomes $V_e = I\rho/4\pi r$, in which $I$ (unit, A) is the current amplitude of the point source and $r$ (unit, m) is the distance from the current source to the measurement site, *i.e.*, the spatial scaling of $V_e$ is inversely proportional to the distance from the current source $I$. We tested the conductivity characteristics of the extracellular milieu in length scales relevant to neurons (*i.e.*, tens of $\mu$m) and realistic current sinks and sources (*i.e.*, membrane currents of identified neurons during spiking) by plotting the mean EAP-amplitude measured from the 8 electrodes along the closest shank at $t_{spike}$ as a function of distance from the cell body (see Materials and Methods). As expected, EAP-amplitude decreases for increasing distance (Fig. 2, a-d, right column; circles: mean EAP-amplitude).

As observed, at $t_{spike}$, EAP-amplitude decays as a monopole (Fig. 2, right column; broken line: least-squares fit of $1/r$-function). To quantify $\rho$ we fit $V_e(t_{spike}) = I(t_{spike})\rho/4\pi r$ where $I(t_{spike}) = -CdV_i(t_{spike})/dt$ with $C$ (unit, F) being the cell capacitance and $V_i$ (unit, V) the intracellular somatic voltage as measured by the patching pipette. The cell capacitance $C$ and resistance $R$ were measured for each cell by injecting an intracellular subthreshold current and fitting the membrane response to an $RC$-response. It has been shown that -$CdV_i(t_{spike})/dt$ satisfactorily approximates spike-related currents $I(t_{spike})$ (Harris et al., 2000) and we found this to hold for the first 0.5-1 ms after $t_{spike}$ (data not shown). Based on the aforementioned, we determined the extracellular resistivity $\rho$ (unit, $\Omega$ m) for 9 L23 pyramidal neurons (red), 4 L4 pyramidal neurons (blue) and 12 L5 pyramidal neurons (black) and found it to be $\rho_{L23PC} = 2.9\pm2.5$ $\Omega$ m, $\rho_{L4PC}$=1.4±1.1 $\Omega$ m and $\rho_{L5PC}$=2.3±4.2 $\Omega$ m (Fig. 2e, left; mean±std). (The main reason for the larger std is problematic estimation of $C$ rather than poor EAP distance-scaling.) A statistically significant difference in resistivity was measured between $\rho_{L23PC}$ and $\rho_{L4PC}$ (ANOVA, $p$ <0.05) with the rest of comparisons being statistically insignificant.

We also report the Pearson correlation as a measure for the quality of fit (qof; 0: no correlation, 1:

perfect fit; mean±std) of the spatial scaling of the EAP-amplitude to the point-source approximation. As observed, there is good agreement between the measured spatial scaling of EAP-amplitude and point-source approximation (Fig. 2e, right). Based on the point-source approximation, ratio $R = V_e/I = \rho/4\pi r$ can be calculated as well as distances $r_{50}$ and $r_{10}$ from the soma where the EAP-amplitude is reduced to half and a tenth, respectively, the EAP-amplitude at 10 $\mu$m ($r_1$) away from the cell body (Fig. 2f). (Notably, this depiction assumes identical current source $I$ for all cell types.)

## Temporal features of EAPs

So far, our analysis based on extracellular signals measured at one instant, $t_{spike}$. Yet the EAP-waveform does not only have spatial features, it also has temporal ones. What are the temporal EAP-characteristics and, importantly, what is their variation? For example, while the most salient feature of the intracellular (extracellular) spike-waveform is the transient, approx. 0.5 to 1 ms-long, Na- and K-dependent positivity (negativity), analyzing the recorded waveforms reveals that spectral content of spikes is significantly stronger at lower frequencies than in the 500-2000 Hz range of the spectrum. Furthermore, pyramidal neurons have consistently slower AP- and EAP-waveforms than basket cell interneurons (Fig. 3a; blue: mean $V_i$; red: strongest EAP-signals from the left and right part of the shank closest to the soma), an observation in agreement with previous studies (Pettersen and Einevoll, 2008; Schomburg et al., 2012) (though see also (Vigneswaran et al., 2011)).

To study temporal EAP-features, we focus on the EAP-signature as recorded along each side of the shank nearest to the patched neuron. Specifically, we normalize the EAP-amplitude across sites and study the time differences in EAP-minima along each shank side (Fig. 3b; black line designates EAP-minimum for recorded signals). We have two definitions of time delay: the first uses $t_{spike}$ as measured intracellularly as time reference (Fig. 3c; black) while the second uses the time $t_{EAP}$ of the minimum of the largest EAP-deflection (Fig. 3c; cyan). The temporal delay between EAPs along the shank is typically smaller than 0.4-0.5 ms. Since the location and inter-electrode distances along a shank are known, we can calculate the velocity $v$ of the EAP-signal propagation by dividing the inter-electrode distance $\Delta x$ by the (absolute) time delay $\Delta t$ of EAP-negativities, $v = \Delta x/\Delta t$ (Fig. 3d). Once more, we have two definitions of velocity: the first takes $\Delta t$ to be the time difference between EAP-negativities across successive electrodes (Fig. 3d, black) while the second takes $\Delta t$ to be the time difference between the EAP-negativity of each electrode and the one of the strongest EAP (Fig. 3d, cyan). Both velocity definitions result in similar outcomes, *i.e.*, the EAP-signal propagation velocity of spikes along the shank for all cells is approx. 0.5-2 mm ms$^{-1}$.

How do such temporal EAP-delays and -propagation arise? One hypothesis is that the extracellular medium has both a resistive and a capacitive component with the latter giving rise to temporal delays in the propagation of the EAP-signal from the soma to the extracellular site (Ranck, 1963; Gabriel et al., 1996; Bédard et al., 2004; Bédard and Destexhe, 2009). Given the measured extracellular resistivity, the extracellular medium would need to have a capacitance of approx. $10^{12}$ F $m^{-1}$ to give rise to the time delays typically observed along a shank which is orders of magnitude greater than estimates of extracellular capacitance (see Discussion for details) (Koch, 1999). Furthermore, such large capacitances would show up in a loss of high-frequency components in the EAP, which is not the case as seen in Fig. 3a. While we cannot exclude the possibility of some extracellular capacitive components, at least for spiking, our experiments suggest that such effects are small.

An alternative hypothesis is that action potentials elicited at the axon initial segment propagate back into the dendrites (Stuart et al., 1997; Shai et al., 2014, 2015; Koch, 1999). In this case, extracellular sites closer to dendrites than the soma (especially sites closer to the thick main apical dendrite, Henze and Buzsaki, 2001) record backpropagating action potentials rather than directly somatic ones. A first indication in support of this hypothesis is that the time delay definition with reference to the minimum of the strongest downward EAP-deflection (Fig. 3c, cyan) is in the vast majority positive, suggesting the site closest to the cell body precedes the EAP-deflection in other sites. Moreover, the same delay definition gives rise to fairly monotonic trends which, given the sites of the shank typically closest to the cell body, are the ones on the edge (sites 4 and 5 in Fig. 2, b-d). This points to the traveling nature of the signal. An additional indication is that the point-source approximation quantitatively fits the EAP-amplitude *vs.* distance relationship only for the spike initiation time. When the same relationship is plotted for the overall EAP-amplitude, *i.e.*, the EAP-amplitude for all times (and not specifically the spike initiation time) along the shank, the quality of fit of the point-source approximation attenuates, suggesting EAP-delays are predominantly attributed to spike backpropagation.

To further assess this hypothesis, we performed simulations using a biophysically and anatomically faithful model of rat somatosensory L5 pyramidal neurons that supports backpropagating action potentials (Hay et al., 2011) (see Experimental Procedures). As in our experimental setup, we inject current steps into the somatic compartment of the model (Fig. 3e; blue: $V_i$ response to current injection) and calculate $V_e$ under the assumption of a purely resistive medium (Holt and Koch, 1999; Gold et al., 2006; Pettersen and Einevoll, 2008; Reimann et al., 2013, $\rho$=2.5 $\Omega$ m) at locations very similar to the position of the silicon probe shank in an experiment with the L5 pyramidal neuron shown in Fig. 1c (Fig. 3e, middle red trace). In another approach, we compute $V_e$ by only considering the contribution of the somatic compartments (Fig.

3e, bottom red trace). Following Fig. 3b, we calculate the mean EAP-waveform for the eight recordings based on the intracellular spike time $t_{spike}$, four for each side of the shank, and normalize the EAP-amplitude (Fig. 3f; red: mean; black line designates EAP-minimum for all recorded signals). While for the EAP-signal contributed from the whole neural morphology, time delays in the EAP-minimum appear, this is not the case for the EAP-signal contributed from the soma only. Moreover, the time delays observed in the simulation are very similar to the ones measured in our experiments (compare Fig. 3b, case L5PC with Fig. 3f, top).

## Changes in the EAP-waveform as a function of firing rate and spiking order

Beyond temporal delays of EAP-negativities along a single shank, extracellular spike waveforms show considerable variability even when recordings are performed from a single spiking cell and the same extracellular recording site (Hill et al., 2011), with such variability particularly enhanced during bursting, *i.e.*, high frequency (>200 Hz) spiking, of cortical neurons (Buzsáki et al., 1996; Henze et al., 2000; Harris et al., 2003). Yet, bursts are comparatively rare events. What is the inherent variability of the EAP-waveform as a function of neural activity? This question has been difficult to address *in vivo* given there is no obvious way of discriminating 'natural' EAP-variability from other occurrences such as electrode displacement, motion artifacts and coupling to electric fields associated with muscular activity (Schomburg et al., 2014).

We investigated the extent to which the EAP-waveform changes as a function of spike rate. That is, we ascribed an interspike interval (ISI) to every spike (ISI-definition: time difference between the previous and the current spike) with spike times determined from the intracellular somatic recording. Stimulation of the whole-cell patched neurons with dc intracellular stimuli of varying strength resulted in Gaussian-like spike frequency-histograms with spike frequency defined as 1/ISI (Fig. 4a; blue: intracellular voltage; red: extracellular trace from the closest electrode to the soma; black: ISI-histogram of a L5 pyramidal neuron).

We assessed both intracellular and extracellular spike waveforms from the same cell for different spike frequencies. We focus on five EAP-characteristics: (1) the initial capacitive positivity ($V_{e,cap}$) amplitude, (2) the EAP-negativity amplitude ($V_{e,extr}$), (3) the EAP-repolarization positivity ($V_{e,repol}$) amplitude, (4) the EAP repolarization time $\tau_e$, and (5) the EAP half-width $\Delta t_{e,hw}$ at half height (Fig. 4b; all features designated in red). Concurrently, we report the correlates of intracellular spike waveforms of the aforementioned features: (1) the change in intracellular voltage spike threshold compared to the mean, (2) the intracellular spike-amplitude ($V_{i,extr}$), (3) the intracellular post-spike negativity ($V_{i,repol}$)-amplitude (compared to baseline), (4) the intracellular spike repolarization time $\tau_i$, and (5) the intracellular spike half-width $\Delta t_{i,hw}$ (Fig. 4b; all features designated in blue). In Fig. 4c we show how these spike-waveform characteristics change

with spike frequency for a single L5 pyramidal neuron (spike frequency histogram shown in Fig. 4a). Note how EAP-amplitude characteristics (in red) vary more with spike frequency than their intracellular correlates (in blue). For example, while $V_{e,extr}$=102±14 $\mu$V (mean±std), $V_{i,extr}$=61±3 mV with the coefficient of variation (COV, defined as the ratio between the std and mean) being 0.14 *vs.* 0.05, *i.e.*, almost three times larger for $V_{e,extr}$ than for $V_{i,extr}$. On the other hand, variability in extracellular temporal-characteristics is broadly similar to their intracellular correlates. For example, for $\Delta t_{e,hw}$ and $\Delta t_{i,hw}$ the COV is 0.16 *vs.* 0.24, revealing larger variability in the temporal characteristics of intracellular than extracellular spikes. Interestingly, it was recently shown that intrinsic biophysical mechanisms are activated along the dendrites of CA1 pyramidal neurons in theta and gamma bandwidths (Vaida and Johnston, 2013). In our experiments we observed consistent changes in EAP-features (most visible in $V_{e,extr}$ and $V_{e,repol}$) in the theta frequency bandwidth (4-12 Hz).

In Fig. 4d-f, we report how spike waveform characteristics change as a function of spike frequency with reference to the mean waveform across all spikes from an individual neuron, irrespective of spike frequency for (top to bottom) 8 L23 and 12 L5 pyramidal neuron recordings as well as 4 basket cell recordings. We report the *relative error* for each feature. For example, for the EAP-amplitude, we report ratio $V_{e,extr}$ - $< V_{e,extr} >/< V_{e,ampl} >$ with $V_{e,extr}$ being the EAP-amplitude in a particular spike frequency bin and $< V_{e,ampl} >$ the mean EAP-amplitude across all spikes. We express the ratio in form of percentual change (line: mean; error bar: std; red: extracellular feature; blue: intracellular feature). As observed, there is substantial variation in the two most salient EAP-features, the EAP-amplitude $V_{e,extr}$ (Fig. 4d-f, second column) and the EAP-repolarization amplitude $V_{e,repol}$ (Fig. 4d-f, third column) for all cell types. Importantly, the relative error in these features is consistently larger in the extracellular rather than the intracellular waveforms (compare red to blue) and non-monotonic as a function of spike frequency. On the other hand, the relative error in repolarization time shows larger variability in intracellular than extracellular spike waveforms while being similar for the halfwidth time. We did not find any distinguishing differences in relative error between cell types.

Transient membrane conductances such as sodium inactivation and slower calcium-dependent currents can alter spike shape (Buzsáki et al., 1996; Henze et al., 2000). In Fig. 5a, intracellular stimulation of varying strength (top: weak; bottom: strong) yields spike trains of approx. 3 (top) and 10 Hz (bottom) for a L5 pyramidal neuron. While for weak stimuli there is little variation in intra- and extracellular spike waveforms (dashed lines: amplitude-range), for strong stimulation the amplitude of the spike waveform (especially the extracellular) changes substantially between the first and subsequent spikes despite their similar ISIs. To quantify such intra- and extracellular spike waveform variability, we repeated the same somatic injection

multiple times, calculated the mean waveforms of the first, second, third, etc. spike, and subtracted them. Using this procedure, we calculate the mean difference between intra- and extracellular spike waveforms as a function of spike occurrence for weak and strong stimulation (Fig. 5b). In Fig. 5c we report the change (relative error) in (left) intra- ($V_{i,extr}$, blue) *vs.* extracellular amplitude ($V_{e,extr}$, red) and (right) halfwidth ($\Delta t_{i,hw}$ *vs.* $\Delta t_{e,hw}$) as a function of spike order comparing the first ten spikes to the 11th for weak (top) and strong (bottom) stimulation. For example, to calculate the relative error in $V_{e,extr}$-amplitude for a particular stimulation strength, we calculate ($V_{e,extr}$-$V_{e,extr}^{11th}/V_{e,extr}^{11th}$) with $V_{e,extr}$ being the EAP-negativity (as defined per Fig. 4) for each of the spike order-bins and $V_{e,extr}^{11th}$ being the EAP-negativity of the 11th spike bin. It is observed that for increasing spike order, EAP-amplitude decreases and EAP-width increases, that is, EAPs becomes smaller and wider. Moreover, compared to the intracellular waveform, the decrease in amplitude and increase in width is much enhanced. In Fig. 5d, we assess this observation for the spike amplitude by fitting the data shown in Fig. 5c (left) with a linear function (least-squares fit with $y = ax + b$ where $a$ is the slope and $b$ the offset) and report the normalized slope $a/b$ for L23 (top) and L5 (bottom) pyramids for intra- (blue) and extracellular (red) spike waveforms as a function of stimulus amplitude. For both cell types the rate of amplitude change is negative, *i.e.*, intra- and extracellular spike amplitude decreases as a function of spike order. Moreover, for L23 pyramids, for weak and strong stimulation, the rate of decrease (slope) does not differ significantly between intra- and extracellular spikes. This is not the case for L5 pyramids where for strong stimulation, the intra- and extracellular spike amplitude decrease is significantly (ANOVA, $p$ <0.05) different, suggesting that the decrease in EAP-amplitude does not proportionally reflect the intracellular one. Such observations are partly attributed to the fact that EAPs reflect both somatic and dendritic, i.e. distributed and inhomogeneous, electrogenesis (Koch, 1999).

What is the spatial dependence of these observations? In Fig. 5e (left two panels) we show the mean CSD of the 2nd *vs.* 11th spike for weak (top) and strong (bottom) stimulation (same L5 pyramid as in panels (a-b); see rightmost traces in panel (b) for EAP-differences) and show their difference in Fig. 5e (rightmost panels). By subtracting CSDs of the same neuron for different spike occurrences it becomes evident that, for the particular L5 pyramid, strong stimulation and fast spiking results in a different spatiotemporal CSD-constellation compared to weak stimulation and slow spiking. To quantify these differences, we fit a 2-dimensional Gaussian function $G(x,t) = A_{CSD} \exp\left(-\frac{(t-t_0)^2}{2\sigma_t^2} - \frac{(x-x_0)^2}{2\sigma_x^2}\right)$ 1 ms around $t_{spike}$ (Fig. 5e, time=0) and plot the relative error (Fig. 5f; left to right) in CSD-amplitude ($A_{CSD}$), space ($\sigma_x$) and time ($\sigma_t$) constant as a function of spike occurrence with reference to the $11^{th}$ spike (Fig. 5f; black: strong stimulation; cyan: weak stimulation; same colored lines: results for both sides of the shank closest to soma; data from same cell as in panels a-c). While changes in spatial and temporal constant broadly existed, the

most sensitive parameter to the spike order for weak *vs.* strong stimulation is the CSD-amplitude that, in the case of strong stimulation, changed by approx. 60% for that neuron. To assess this effect quantitatively, we follow the method introduced in panels (c-d) and fit the CSD-amplitude *vs.* spike order-data with a linear function for a set of L23 and L5 pyramidal neurons and report the normalized slope (Fig. 5g). We do so for the CSD amplitude change (red) as a function of cell type (L23 *vs.* L5 pyramids), shank side (CSD calculated from the four electrodes on the same *vs.* the opposite side the cell body), stimulation amplitude (weak *vs.* strong) and compare it with the $V_{i,extr}$-change (blue; same data as in panel (d)). The negative value of the slopes illustrates that also CSD-amplitude decreases with spike order. Yet, unlike in panel (d), the comparison between $V_{i,extr}$-amplitude-slope and CSD-amplitude-slope is statistically insignificant, suggesting that (unlike for $V_{e,extr}$ of L5 pyramids shown in panel (d)) CSD-amplitude decrease reflects the measured $V_{i,extr}$-decrease. These observations remain broadly similar for L23 and L4 pyramids.

Fig. 4 and 5 suggest that the relationship between the EAP-waveform and $V_i$ is complicated. In fact, biophysical considerations support that the negative derivative of the intracellular potential is proportional to the EAP-waveform (Koch and Laurent, 1999). To assess this, in Fig. 6 we plotted the amplitude-normalized -d$V_i$/dt and the EAP-waveform for (top to bottom) a L23 and a L4 pyramid as well as for a basket cell (same cells as in Fig. 2). We show this relationship for increasing (left to right) spike rates (with the spike rate assessed the same as in Fig. 4). Indeed, the two waveforms are qualitatively similar in shape (importantly, not in absolute amplitude) during the initial Na- and K-component of the spike. The comparison becomes poorer after the EAP-negativity when slower, repolarizing currents are activated that cannot be captured by simply differentiating $V_i$. Concurrently, during such later stages of spike initiation, charge transfer is no more confined perisomatically but has propagated along the morphology casting the entire neuron a spatially distributed sink/source contributing to the extracellular potential.

## Low-frequency contributions of EAPs

Recent computational (Denker et al., 2011; Schomburg et al., 2012; Reimann et al., 2013) and experimental *in vivo* (Ray and Maunsell, 2011; Belluscio et al., 2012) studies support the notion that extracellular spike waveforms not only contribute to the higher-frequency portion of $V_e$-recordings but also impact lower bandwidths. Addressing and quantifying such effects has proven difficult, especially since capturing the slower, mostly repolarizing, spike currents of smaller amplitude is challenging.

We used the spike-triggered average EAP-waveforms from identified cells (Fig. 7a, red) to construct fictitious extracellular traces and analyze their power with and without spikes. Nine second-long $V_e$-recordings

from an extracellular site far from the patched neuron that did not detect any spiking (as assessed from the STA) was the baseline. To this, EAP-waveforms at ISIs drawn from a log-normal distribution (Mizuseki and Buzsáki, 2013; Buzsáki and Mizuseki, 2014) with mean spike frequency $f_0$ were added at three spike rates, $f_0$=1, 8 and 30 Hz (Fig. 7b). In a next step, we calculated 50 realizations for each $f_0$ which resulted in 50 unique (Fig. 7c-e) 9 s-long extracellular traces. We then calculated their spectral content (Fig. 7f; line: mean spectral power from 50 traces using the EAP of a L5 pyramidal neuron shown in panel a1; green: no spiking; red: $f_0$=1 Hz spiking, black: $f_0$=8 Hz; blue: $f_0$=30 Hz). As observed, there is substantial deviation in spectral power between the spiking and no- or low-spiking traces at frequencies as low as 20 Hz.

What part of the EAP-waveform can impact power at such low frequencies? To address this question, we performed so-called 'de-spiking', *i.e.*, we substituted a window of 0.6 ms before and after the spike initiation time $t_{spike}$ with a spline fit (Belluscio et al., 2012). This resulted in EAP-waveforms lacking the typical spike-negativity but containing the repolarization (Fig. 7a; de-spiked EAP-waveform in black). We calculated the spectral power for the same $f_0$ using the de-spiked waveforms (Fig. 7g) and confirmed our previous conclusion: reasonably high spiking impacts spectral power as low as 20 Hz compared to no or low spiking. Moreover, we attribute the difference in frequency-scaling between intact and de-spiked waveforms beyond 50 Hz to the impact of the EAP-negativity (compare Fig. 7f and 7g). Importantly, when performing the same analyses using the EAP-waveform from basket cells (Fig. 7, a3 and a4), the outcome is very different: spiking minimally contributes to spectral power under approx. 100 Hz and, even then, does so only for elevated spike frequencies (Fig. 7h). We attribute the lack of impact of basket cell spiking to LFPs below 100 Hz to their temporally narrow EAP-waveform as well as the lack of long-lasting depolarizing currents (compare intracellular waveforms between Figs. 2a-c and 2d). The conclusions for Figs. 7f-h are supported by statistical tests ($t$-testing) we performed (Figs. 7i-k) where spectral power between no spiking (control) and spiking cases (red: comparison between control and 1 Hz spiking; black: comparison between control and 8 Hz spiking; blue: comparison between control and 30 Hz spiking) was pairwise-compared at various frequencies (steps of 5 Hz; null-hypothesis: spectral power between spiking traces and controls are drawn from the same distribution; dashed lines: $p$=$10^{-3}$, Bonferroni-corrected for multiple comparisons). As observed, for EAPs from a L5 pyramidal neuron, spiking significantly impacts spectral power of the extracellular recording as low as 20 Hz for $f_0$ greater than 1 Hz (Fig. 7i), an observation mainly attributed to repolarization currents as the difference remains when EAP-negativities have been removed (Fig. 7j).

Of course, extracellular electrodes usually pick up EAPs from multiple neurons. Indeed, they typically record larger amplitude EAPs (larger than 50 $\mu$V amplitude) from only a few individual neurons located very closely and smaller-amplitude EAPs from many more located in the greater vicinity (Buzsaki, 2004;

Holt and Koch, 1999; Gold et al., 2006; Schomburg et al., 2012) (see also Fig. 2). To account for this, in Fig. 7l-n we performed the same analyses as in Fig. 7i-j but instead of using the EAP-waveform from a single neuron we used EAP-waveforms from multiple cells. To do so, we define the overall spike frequency $f_{MUA}$ attributed to spiking from all cells (equivalent to multi-unit activity or MUA) and at each ISI (drawn from a log-normal distribution; Fig. 7c-e) we sum the EAP-waveform of a randomly chosen neuron (of the same cell type) from 8 L23 pyramidal neurons (Fig. 7, l-n, leftmost), 4 L4 pyramidal neurons (Fig. 7, l-n, middle) and 12 L5 pyramidal neurons (Fig. 7, l-n, rightmost) with a control trace (recorded from far away) for spike rate $f_{MUA}$=8, 32 and 96 Hz (in each of panels l-n, from left to right). The resulting $V_e$-traces (similar to the ones shown in Fig. 7b) contain EAP-waveforms from many neurons of a particular type. We show the statistical significance ($t$-test, dashed line: $p < 10^{-3}$, Bonferroni-corrected for multiple-comparisons) of the difference in spectral power between control (no spiking) and spiking traces at different frequencies (steps of 5 Hz; null-hypothesis: spectral power between control and spiking traces are drawn from the same distribution) for intact (red) and de-spiked (black) EAP-waveforms. As observed, while for $f_{MUA}$=8 Hz (equivalent to 8 neurons spiking at 1 Hz) spiking does not substantially impact spectral power below 100 Hz, for faster (but still very realistic) rates of $f_{MUA}$=32 and 96 Hz, spiking profoundly impacts spectral power at frequencies as low as 20 Hz. This is especially true for L4 and L5 pyramidal neurons. We also studied the effect of different EAP-waveforms as measured by different sites along the shank by considering the strongest, second and third strongest EAP-signals, both for the intact and de-spiked EAP-waveforms (Fig. 7l-n, three lines of the same color). While the strongest EAP-waveforms (cell-type: mean EAP-amplitude±std; L23PC: 39±10 $\mu$V; L4PC: 57±35 $\mu$V; L5PC: 51±61$\mu$V) impact spectral density at low frequencies already for $f_{MUA}$=32 Hz, broadly the same effects hold even when considering the second strongest EAP-waveforms of the same neurons (cell-type: mean EAP-amplitude±std; L23PC: 32±7 $\mu$V; L4PC: 30±4 $\mu$V; L5PC: 40±10 $\mu$V).

# Discussion

Assessing the neural origins of electric signals has remained problematic even if the biophysical laws governing the initiation and propagation of these electric events are well understood (Mitzdorf, 1985; Logothetis and Wandell, 2004; Buzsáki et al., 2012; Einevoll et al., 2013). Our experimental setup allows us to access intracellularly and whole-cell patch-clamp somata of identified neurons located a few tens of $\mu$m away from extracellular silicon probes of known spatial constellation. By stimulating these identified neurons through intracellular dc current injections and eliciting spikes, we recorded intracellular and extracellular spiking signals. Notably, access to the intracellular voltage allows precise detection of spike times, alignment

of intracellular and extracellular voltage traces and obtention of reliable intracellular and extracellular spike-triggered averages (STA). The latter is essential to our study as it allows experiment- (distance to extracellular recording sites) and cell type-specific (extracellular resistivity, slow *vs.* fast spiking) comparisons while doing away with the ambiguity of thresholding and origin (single *vs.* multiple neurons) of these signals. Using these experiments we addressed three questions: the spatial EAP propagation in cortical matter, temporal effects of EAPs and spike contribution to the local field potential (LFP).

## Spatial EAP propagation

To assess the physical properties of the extracellular medium such as the extracellular resistivity and characterize the EAP-spread, we used a phenomenological model treating electrogenesis along the entire morphology at $t_{spike}$ as a point source. While this way a number of processes and features are lumped into a single parameter/point, such an approximation offers many advantages over alternative experiments using microwires or parallel plates (Ranck, 1963; Gabriel et al., 1996; Logothetis et al., 2007; Anastassiou et al., 2011) that lack spike-related electrogenesis. The use of the silicon probe allowed us to quantify the spatial spread of EAP-signals at the microscopic level. We found that, at spike initiation time, the point-source approximation in a resistive medium (Holt and Koch, 1999) captures the spatial decay of the EAP-amplitude. Furthermore, by assuming current generation as the negative product of a cell's capacitance and the intracellular somatic derivative (Koch, 1999), we calculated the microscopic, layer-specific extracellular resistivity and found it to be in agreement to studies quantifying it at the meso- and macroscopic level (Logothetis et al., 2007; Goto et al., 2010).

## Temporal effects of EAPs

We sought to understand variations in the extracellular spike-negativity. We measured propagation delay and velocity along the silicon probe and found it to be in agreement with measurements of backpropagating action potentials (Stuart et al., 1997; Buzsáki et al., 1996; Buzsáki and Kandel, 1998; Henze et al., 2000; Blanche et al., 2005). Thus, we attribute such temporal variations to the contribution of dendritic compartments to the extracellular spike signal. This finding is seemingly in variance with the biophysical simulations of Gold and colleagues (Gold et al., 2006) who suggested that it is mainly the cell body and proximal thick dendrites that affect the recorded EAP-waveform. While true that the main contributor of the EAP-waveform are perisomatic compartments of a neuron, more distal dendritic compartments also contribute to the recorded signal. In fact, our simulations suggest that only accounting for perisomatic compartments

does not re-produce the observed time delays while strongly overestimating EAP-amplitude close to the soma. Our findings are in line with computational (Pettersen and Einevoll, 2008; Schomburg et al., 2012) and experimental (Buzsáki et al., 1996; Buzsáki and Kandel, 1998; Henze et al., 2000; Blanche et al., 2005) work supporting the contribution of dendritic transmembrane currents to EAPs.

It has been hypothesized that temporal delays of EAPs can also appear if the extracellular medium has a capacitive component (in addition to its resistive nature) (Gabriel et al., 1996; Bédard et al., 2004; Bédard and Destexhe, 2009). The main argument in favor of such a hypothesis is that the gray matter of cerebral cortex is filled with cellular membranes with the extracellular fluid taking up a fairly small volume (0.05-0.15) (Lopez-Aguado et al., 2001). Given the measured extracellular resistivity (approx. 2.5 $\Omega$ m) and the measured temporal delay (approx. 0.3 ms) observed in spike-negativity along a shank, assuming simple $RC$ circuit formalism the extracellular medium would need to have a capacitance of approx. $10^{12}$ F $m^{-1}$. This is orders of magnitude larger than the membrane capacitance (Koch, 1999). In fact, our data support that local, compartmental electrogenesis such as backpropagating action potentials (APs) through dendrites impact EAP-features such as amplitude and time-delays rather than extracellular capacitance filtering. Yet, we cannot exclude that for larger distances and different/stronger current sources, there might be a capacitive feature (Bédard et al., 2004).

Yet, is the fact that the point-source approximation is a good fit for EAP distance-scaling at $t_{spike}$ not at odds with our observation that the whole cell morphology contributes to the EAP-waveform? The short answer is no. Importantly, the point-source approximation (as presented in Fig. 2) is an apparent or phenomenological model of EAP-distance scaling. Following the same argument, the extracellular resistivity as reported in Fig. 2 is a phenomenological property. By no means does such a model suggest that a single compartment contributes to the EAP nor should it encourage such a simplistic interpretation. Yet, it does give a first-order response to the question: given a certain distance between the cell body and the electrode, what is the EAP-spread? Clearly, in order to address such a question in its entirety, a sophisticated 3-dimensional model would be required that can fully simulate all electrogenesis (and its heterogeneity) in the intracellular, transmembrane, and extracellular space as well as in/around the recording electrode. As such, our phenomenological point-source model based on measured properties provides a useful first-order approximation, for example, for EAP-spread (Fig. 2f).

An important aspect of extracellular recordings is their inherent, activity-dependent variability. Indeed, the EAP-amplitude of hippocampal pyramidal neurons can vary as much as 60% during a high-frequency (more than 200 Hz) burst (Buzsáki et al., 1996), for example within a place field (Harris et al., 2001). These

features, together with artifactual sources of variability from electromyogram contamination or hardware sources pose challenges for spike waveform-based clustering and classification of neurons *in vivo*. Our *in vitro* measurements present advantages over *in vivo* recordings, since variability of the EAP-waveform is not affected by fluctuations of the membrane potential and spiking activity of other neurons. We chose spike frequency as an independent variable as *in vivo* measurements indicate that slow spiking gives rise to more stereotypical EAP-waveforms than fast rates, e.g. during burst firing (Buzsáki et al., 1996; Harris et al., 2001). We report that the most salient features of EAPs, the EAP-negativity attributed to fast sodium- and potassium-dependent currents and the immediately proceeding EAP-positivity attributed to slower potassium (but also calcium) currents, can substantially vary as a function of spike frequency. In general, we found that spike variability of the EAP-amplitude is more pronounced compared to intracellular spike variability (Henze et al., 2000), is non-monotonic as a function of spike frequency and is present in all cell types we studied. The temporal EAP-features, such as halfwidth or decay time of spike repolarization, varied more reliably with the intracellular waveform than the amplitude (Bartho et al., 2004).

We also analyzed EAP-features as a function of spike order (first *vs.* second *vs.* third spike) and found that EAP-amplitude of L5 pyramids decreased with spike order significantly more than the intracellular spike amplitude, an observation already established *in vivo* for CA1 pyramidal neurons (though for much higher spike rates) (Buzsáki et al., 1996). Such observations support the notion that perisomatic and, in fact, dendritic electrogenesis can vary and that a cascade of time-dependent and spatially distributed events are reflected in the EAP, much more so than in the intracellular somatic recordings of spikes (Gold et al., 2007; Anastassiou et al., 2013). Additionally, while EAP-amplitude decrease cannot account for intracellular spike amplitude change (even if only for L5 pyramids) CSD-amplitude decrease can, suggesting that single neuron CSDs or, alternatively, detection of spikes of individual neurons from multiple extracellular electrodes at known locations yields more robust spike measurements.

Finally, based on passive cable theory (Rall, 1977), assuming an intracellular current injection $I_{inj}$ at a specific location along a patch of membrane, the membrane current per unit length of cable, $i_m(x,t)$, is given by

$$i_m(x,t) = \frac{V_m(x,t) - V_{rest}}{r_m} + c_m \frac{\partial V_m(x,t)}{\partial t} - I_{inj}(x,t)$$

where $V_m$ is the membrane potential at location $x$ and time $t$, $V_{rest}$ the resting potential, $r_m$ the membrane resistance of unit length cable and $c_m$ the membrane capacitance per unit length. We observe that $i_m$, i.e. the source term of extracellular signals such as the EAP (Holt and Koch, 1999; Gold et al., 2006; Anastassiou et al., 2013), is proportional to the temporal derivative of $V_m$ which, in this case, can be approximated by the

intracellular potential, $V_i$. One important implication is that the timing of the positivity of the intracellular spike does not coincide with the EAP-negativity. Assuming resistive extracellular conductivity, it follows that $i_m$ is the source of the $V_e$-signal so that $i_m$ and $V_e$ are completely in-phase. It also follows that $V_i$ ($V_m$) and $i_m$ have an $RC$-type relationship, i.e. there is a phase between them. Thus, in terms of timing, $V_i$ (or $V_m$) and $V_e$ will not be in-phase (e.g. see Fig. 2 and 4b). In fact, the EAP-negativity from a signal recorded close to the soma broadly corresponds to the maximum rate of rise of the intracellular spike and thus typically precedes the intracellular spike positivity (see Fig. 6 and (Buzsáki et al., 1996; Henze et al., 2000)). Further away from the soma, electrogenesis of local membranes can impact the EAP-waveform so that the time-correspondence between EAP- and intracellular somatic spike-features may become further obscured. In addition, experimentally, the similarity between the EAP-waveform and the temporal derivative of $V_i$ remains qualitative especially after the initial phase of the action potential generation casting the $V_i$-derivative as a rather coarse approximation of the EAP-waveform.

## Spike contribution to the LFP

Unit activity is traditionally thought to impact the high-frequency (above 500 Hz) spectrum of extracellular recordings. The low-pass filtered part of the extracellular signal, the so-called local field potential (LFP), has historically been considered to mainly reflect a combination of postsynaptic activity and associated currents such as return currents as well as other processes such as oscillatory membrane and calcium-dependent currents (Mitzdorf, 1985; Logothetis et al., 2007; Buzsáki et al., 2012; Einevoll et al., 2013). Recent computational and experimental studies have challenged this picture by showing that spike currents can impact bandwidths of the extracellular signal in the traditional LFP band (below 100 Hz, Rasch et al., 2009; Ray and Maunsell, 2011; Belluscio et al., 2012; Zanos et al., 2011; Schomburg et al., 2012; Reimann et al., 2013; Waldert et al., 2013). Though interpretation of single-neuron CSD analyses is somewhat ambiguous, our experiments are in agreement with simulations (Pettersen and Einevoll, 2008; Schomburg et al., 2012) showing that extracellular spikes can impact bandwidths lower than 200 Hz. Yet, the extent to which spiking can impact LFP-characteristics has remained speculative. Our intracellularly induced spikes show that EAPs and spike afterpotentials of L4 and L5 pyramids can contribute spectral power as low as 20 Hz compared to non-spiking $V_e$-traces. The effect of EAPs in such low frequencies is attributed to the slower, smaller-amplitude repolarization typically difficult to distinguish *in vivo* though synaptic currents may also influence the EAP-waveform in such time scales (Glickfeld et al., 2009).

What are the functional and computational ramifications of this observation? Spike-field coherence (with

certain LFP-bandwidths) is often used to infer the relationship between synaptic input (considered to be reflected in the lower LFP bands) and neural output (spiking) (Fries et al., 1997; Womelsdorf et al., 2006; Montgomery et al., 2008; Rutishauser et al., 2010; Anastassiou et al., 2011). Yet, if spiking itself can impact bands as low as beta or gamma, *i.e.*, LFPs in these bandwidths are also shaped by spiking, then the causal relationship between LFPs (as a proxy to synaptic input) and spiking becomes questionable (Billeh et al., 2014; Anastassiou and Koch, 2015; Schaub et al., 2015). On the other hand, clearly, synaptic currents are required to elicit spiking and will impact LFPs. The extent to which spiking and LFP (even in low bands) are independent is thus state-dependent (for example, slow *vs.* fast background spiking) and measures such as spike-field coherence need to be assessed accordingly.

## Acknowledgments

We thank Aleena Garner, Kenji Mizuseki, Adam Shai and Tim Blanche for comments and discussions. This work was funded by the Swiss National Science Foundation (C.A.A.), the Human Frontier Sciences Program (C.K. G.B. and H.M.), the National Institute of Neurological Disorders and Stroke (C.K.) and the Mathers Foundation (C.K.) C.A.A. and C.K. wish to thank the Allen Institute founders, P. G. Allen and J. Allen, for their support.

# References


**Amzica F, Steriade M**. Neuronal and glial membrane potentials during sleep and paroxysmal oscillations in the neocortex. *J Neurosci* 20: 6648–6665, 2000.

**Anastassiou CA, Koch C**. Ephaptic coupling to endogenous electric field activity: why bother? *Curr Op Neurobiol* 31: 95–103, 2015.

**Anastassiou CA, Perin R, Markram H, Koch C**. Ephaptic coupling of cortical neurons. *Nat Neurosci* 14: 217–223, 2011.

**Anastassiou C, Buzsáki G, Koch C** 2013 *Principles of neural coding*, chapter Biophysics of extracellular spikes, p. 15–37 CRC Taylor.

**Bartho P, Hirase H, Monconduit L, Zugaro M, Harris K, Buzsaki G**. Characterization of neocortical principal cells and interneurons by network interactions and extracellular features. *J Neurophysiol* 92: 600–608, 2004.

**Bédard C, Destexhe A**. Macroscopic models of local field potentials and the apparent 1/f noise in brain activity. *Biophys J* 96: 2589–2603, 2009.

**Bédard C, Kroger H, Destexhe A**. Modeling extracellular field potentials and the frequency-filtering properties of extracellular space. *Biophys J* 86: 1829–1842, 2004.

**Belluscio MA, Mizuseki K, Schmidt R, Kempter R, Buzsáki G**. Cross-frequency phase- phase coupling between theta and gamma oscillations in the hippocampus. *J Neurosci* 32, 2012.

**Billeh YN, Schaub MT, Anastassiou CA, Barahona M, Koch C**. Revealing cell assemblies at multiple levels of granularity. *J Neurosci Meth* 236: 92–106, 2014.

**Blanche T, Spacek M, Hetke J, Swindlale N**. polytrodes: High-density silicon electrode arrays for large-scale multiunit recording. *J Neurophysiol* 93: 2987–3000, 2005.

**Buzsaki G**. Large-scale recording of neuronal ensembles. *Nature Neurosci* 7: 446–451, 2004.

**Buzsáki G, Anastassiou CA, Koch C**. Origin of extracellular fields and currents – eeg, ecog, lfp and spikes. *Nature Reviews Neuroscience* 13: 407–420, 2012.

**Buzsáki G, Kandel A**. Somadendritic backpropagation of action potentials in cortical pyramidal cells of the awake rat. *J Neurophysiol* 79: 1587–1591, 1998.

**Buzsáki G, Mizuseki K**. The log-dynamic brain: how skewed distributions affect network operations. *Nat Rev Neurosci* 15: 264–278, 2014.

**Buzsáki G, Penttonen M, Nádasdy Z, Bragin A**. Pattern and inhibition-dependent invasion of pyramidal cell dendrites by fast spikes in the hippocampus in vivo. *Proc Natl Acad Sci U S A* 93: 9921–9925, 1996.

**Csicsvari J, Henze D, Jamieson B, Harris K, Sirota A, Barthó P, Wise K, Buzsáki G**. Massively parallel recording of unit and local field potentials with silicon-based electrodes. *J Neurophysiol* 90: 1314–1324, 2003.

**Deans J, Powell A, Jefferys J**. Sensitivity of coherent oscillations in rat hippocampus to ac electric fields. *J Physiol* 583: 555–565, 2007.

**Denker M, Roux S, Linden H, Diesmann M, Riehle A, Grün S**. The local field potential reflects surplus spike synchrony. *Cereb Cortex* 21: 2681–2695, 2011.

**Druckmann S, Berger T, Schürmann F, Hill S, Markram H, Segev I**. Effective stimuli for constructing reliable neuron models. *PLoS Comput Biol* 7: e1002133, 2011.

**Du J, Riedel-Kruse IH, Nawroth JC, Roukes ML, Laurent G, Masmanidis SC**. High-resolution three-dimensional extracellular recording of neuronal activity with microfabricated electrode arrays. *J Neurophysiol* 101: 1671–1678, 2009.

**Einevoll GT, Kayser C, Logothetis NK, Panzeri S**. Modelling and analysis of local field potentials for studying the function of cortical circuits. *Nat Rev Neurosci* 14: 770–785, 2013.

**Fries P, Roelfsma PR, Engel A, König P, Singer W**. Synchronization of oscillatory responses in visual cortex correlates with perception in interocular rivalry. *Proc Natl Acad Sci U S A* 94: 12699–12704, 1997.

**Gabriel S, Lau RW, Gabriel C**. The dielectric properties of biological tissues .2. measurements in the frequency range 10 hz to 20 ghz. *Physics Medicine Biology* 41: 2251–2269, 1996.

**Glickfeld LL, Roberts JD, Somogyi P, Scanziani M**. Interneurons hyperpolarize pyramidal cells along their entire somatodendritic axis. *Nat Neurosci* 12: 21–23, 2009.

**Gold C, Henze D, Koch C**. Using extracellular action potential recordings to constrain compartmental models. *J Comp Neurosc* 23: 39–58, 2007.

**Gold C, Henze D, Koch C, Buzsáki G**. On the origin of the extracellular action potential waveform: A modeling study. *J Neurophysiol* 95: 3113–3128, 2006.

**Goto T, Hatanaka R, Ogawa T, Sumiyoshi A, Riera J, Kawashima R**. An evaluation of the conductivity profile in the somatosensory barrel cortex of wistar rats. *J Neurophysiol* 104: 3388–3412, 2010.

**Gray CM, Maldonado PE, Wilson M, McNaughton B**. Tetrodes markedly improve the reliability and yield of multiple single-unit isolation from multi-unit recordings in cat striate cortex. *J Neurosci Meth* 63: 43–54, 1995.

**Harris KD, Henze D, Csicsvari J, Hirase H, Buzsaki G**. Accuracy of tetrode spike separation as determined by simultaneous intracellular and extracellular measurements. *J Neurophysiol* 84, 2000.

**Harris KD, Hirase H, Leinekugel X, Henze DA, Buzsáki G**. Temporal interaction between single spikes and complex spike bursts in hippocampal pyramidal cells. *Neuron* 32: 141–149, 2001.

**Harris K, Csicsvari J, Hirase H, Dragoi G, Buzsaki G**. Organization of cell assemblies in the hippocampus. *Nature* 424: 552–556, 2003.

**Hay E, Hill S, Schürmann F, Markram H, Segev I**. Models of neocortical layer 5b pyramidal cells capturing a wide range of dendritic and perisomatic active properties. *PLoS Computat Biol* 7: e1002107, 2011.

**Henze D, Borhegyi Z, Csicsvary J, Mamiya A, Harris K, Buzsaki G**. Intracellular features predicted by extracellular recordings in the hippocampus *in vivo*. *J Physiol* 84: 390–400, 2000.

**Henze D, Buzsaki G**. Action potential threshold of hippocampal pyramidal cells in vivo is increased by recent spiking activity. *Neuroscience* 105: 121–130, 2001.

**Hill DN, Mehta SB, Kleinfeld D**. Quality metrics to accompany spike sorting of extracellular signals. *J Neurosci* 31: 8699–8705, 2011.

**Histed M, Bonin V, Reid R**. Direct activation of sparse, distributed populations of cortical neurons by electrical microstimulation. *Neuron* 63: 508–522, 2009.

**Holt G** 1998 A critical reexamination of some assumptions and implicatinos of cable theory in neurobiology Ph.D. diss., California Institute of Technology.

**Holt G, Koch C**. Electrical interactions via the extracellular potential near cell bodies. *J Comp Neurosci* 6: 169–184, 1999.

**Koch C** *Biophysics of Computation: Information Processing in Single Neurons* Oxford University Press, Oxford, England, 1999.

**Koch C, Laurent G**. Complexity and the nervous system. *Science* 284: 96–98, 1999.

**Logothetis N, Kayser C, Oeltermann A**. In vivo measurement of cortical impedance spectrum in monkeys: Implications for signal propagation. *Neuron* 55: 809–823, 2007.

**Logothetis N, Wandell B**. Interpreting the bold signal. *Annu Rev Physiol* 66: 735–769, 2004.

**Lopez-Aguado L, Ibarz J, Herreras O**. Activity-dependent changes of tissue resistivity in the ca1 region in vivo are layer-specific: Modulation of evoked potentials. *Neuroscience* 108: 249–262, 2001.

**Mitzdorf U**. Current source-density method and application in cat cerebral cortex: investigation of evoked potentials and eeg phenomena. *Physiol Rev* 65: 37–100, 1985.

**Mizuseki K, Buzsáki G**. Preconfigured, skewed distribution of firing rates in the hippocampus and entorhinal cortex. *Cell Reports* 4: 1010–21, 2013.

**Mizuseki K, Diba K, Pastalkova E, Buzsáki G**. Hippocampal ca1 pyramidal cells form functionally distinct sublayers. *Nat Neurosci* 14: 1174–1181, 2011.

**Mizuseki K, Sirota A, Pastalkova E, Buzsáki G**. Theta oscillations provide temporal windows for local circuit computation in the entorhinal-hippocampal loop. *Neuron* 64: 267–280, 2009.

**Montgomery SM, Sirota A, Buzsáki G**. Theta and gamma coordination of hippocampal networks during waking and rapid eye movement sleep. *J Neurosci* 28: 6731–6741, 2008.

**Nicholson C**. Theoretical analysis of field potentials in anisotropic ensembles of neuronal elements. *IEEE Trans Biomed Eng* 20: 278–288, 1973.

**Patel BA, Anastassiou CA, O'Hare D** 2006 *Body Sensor Networks*, chapter Biosensor design and interfacing, p. 41–87 Springer London.

**Perin R, Berger TK, Markram H**. A synaptic organizing principle for cortical neuronal groups. *Proc Natl Acad Sci U.S.A* 108: 5419–5424, 2011.

**Pettersen KH, Einevoll GT**. Amplitude variability and extracellular low-pass filtering of neuronal spikes. *Biophys J* 94: 784–802, 2008.

**Rall W** 1977 *Core conductor theory and cable properties of neurons*, p. 39–97 Am. Physiological Society, Bethesda, MA.

**Ranck J**. Analysis of specific impedance of rabbit cerebral cortex. *Exp Neurol* 7: 153–174, 1963.

**Rasch M, Logothetis NK, Kreiman G**. From neurons to circuits: linear estimation of local field potentials. *J Neurosci* 29: 13785–13796, 2009.

**Ray S, Maunsell JHR**. Different origins of gamma rhythm and high-gamma activity in macaque visual cortex. *PLoS Biol* 9: e1000610, 2011.

**Reimann M, Anastassiou C, Perin R, Hill S, Markram H, Koch C**. A biophysically detailed model of neocortical local field potentials predicts the critical role of active membrane currents. *Neuron* 79: 375–390, 2013.

**Rutishauser U, Ross IB, Mamelak AN, Schuman EM**. Human memory strength is predicted by theta-frequency phase-locking of single neurons. *Nature* 464: 903–907, 2010.

**Schaub MT, Billeh YN, Anastassiou CA, Koch C, Barahona M**. Emergence of slow-switching assemblies in structured neuronal networks. *arXiv* p. 1502.05656, 2015.

**Schomburg EW, Anastassiou CA, Buzsáki G, Koch C**. The spiking component of oscillatory extracellular potentials in the rat hippocampus. *Journal Neuroscience* 32: 11798–11811, 2012.

**Schomburg EW, Fernandez-Ruiz A, Mizuseki K, Berényi A, Anastassiou C, Koch C, Buzsáki G**. Theta phase segregation of input-specific gamma patterns in entorhinal-hippocampal networks. *Neuron* 84: 470–485, 2014.

**Shai AS, Anastassiou CA, Larkum ME, Koch C**. Physiology of layer 5 pyramidal neurons in mouse primary visual cortex: Coincidence detection through bursting. *PLoS Comput Biol* 11: e1004090, 2015.

**Shai AS, Koch C, Anastassiou CA**. Spike-timing control by dendritic plateau potentials in the presence of synaptic barrages. *Front Comput Neurosci* 8: 89, 2014.

**Stuart G, Schiller J, Sakmann B**. Action potential initiation and propagation in rat neocortical pyramidal neurons. *J Physiol* 505: 617, 1997.

**Vaida SP, Johnston D**. Temporal synchrony and gamma-to-theta power conversion in the dendrites of ca1 pyramidal. *Nat Neurosci* 16: 1812–1820, 2013.

**Vigneswaran G, Kraskov A, Lemon RN**. Large identified pyramidal cells in macaque motor and premotor cortex exhibit "thin spikes": Implications for cell type classification. *J Neurosci* 31: 14235–14242, 2011.

**Waldert S, Lemon RN, Kraskov A**. Influence of spiking activity on cortical local field potentials. *J Physiol* 591: 5291–5303, 2013.

**Womelsdorf T, Fries P, Mitra PP, Desimone R**. Gamma-band synchronization in visual cortex predicts speed of change detection. *Nature* 439: 733–736, 2006.

**Zanos S, Zanos TP, Marmarelis VZ, Ojemann GA, Fetz EE**. Relationships between spike-free local field potentials and spike timing in human temporal cortex. *J Physiol* 107: 1808–1821, 2011.

# Figure legends

**Figure 1:** Intracellular somatic spiking and its extracellular reflection as measured by the 32-site silicon probe recordings in rat somatosensory slices from a (a) L23 pyramidal neuron, (b) L4 pyramidal neuron, (c) L5 pyramidal neuron and (d) L3 basket cell. (Left) Images of the reconstructed neural morphology (dendrites: black; axon: red; horizontal lines indicate cortical layers) and location of silicon probe from individual experiments. (The arrow in panel (a) shows the patched L23 neuron.) Somatic spiking is induced via administration of a suprathreshold 9 s dc intracellular step of variable strength. Administration of small amplitude dc current (weak stimulation) resulted in slow spiking (middle) while an increase in the amplitude (strong stimulation) gives rise to faster spiking (right). Intracellular current stimulus is shown on top (black), intracellular somatic voltage response (blue) in the middle, extracellular voltage (as recorded from electrode of the silicon probe closest to the soma; red) at the bottom.

**Figure 2:** Intra- and extracellular action potentials for the cells shown in Fig. 1 as recorded from the whole-cell patch electrode as well as by eight electrodes along the shank located most proximal to the spiking neuron. (a-d) Spike-triggered intra- and extracellular responses for a (a) L23, (b) L4 and (c) L5 pyramidal neuron as well as (d) a L3 basket cell. (First column) The spike-triggered average of $V_i$ aligned at $t_{spike}$ determined as the maximum of the second time derivative of $V_i$ right before the maximum $V_i$ (blue line: mean; broken line: std). All spike triggered average $V_i$-traces are aligned at $t_{spike}$ (dashed red line). (Second and third column) Spike-triggered average of the recorded $V_e$ (black lines) from the left (second column) and right four electrodes (third column) of the most proximal shank adjacent to the soma (schematized by the triangle). Colors indicate the mean spike-triggered current source density (red: source; blue: sink) attributed to spiking. (Fourth column) EAP-amplitude at $t_{spike}$ as a function of distance between the whole cell-patched soma and extracellular sites along the shank closest to the soma. (e) Extracellular resistivity $\rho$ (left) and quality of fit (right; 0 no correlation and 1 perfect fit) for 9 L2/3 (red), 4 L4 (blue) and 12 L5 (black) pyramidal neurons for the extracellular voltage inferred by assuming a current point source in a purely resistive cytoplasm (see text). Comparison between layer-specific $\rho$ yielded statistically significant difference between $\rho_{L23PC}$ and $\rho_{L4PC}$ (ANOVA, $p$ <0.05). (f) Based on the layer-specific $\rho$ (same color-coding as panel e), the ratio $R = V_e/I = \rho/4\pi r$ is calculated as a function of distance with distances $r_{50}$ and $r_{10}$ designating the distance where the EAP-amplitude becomes 50% and 10%, respectively, compared to the EAP-amplitude 10 $\mu$m ($r_1$) from the cell body.

**Figure 3:** Temporal characteristics of EAP-signals from identified single neurons. (a) Frequency spectra of intracellular spikes (blue lines) and the two largest EAPs (red lines) of the four neurons shown in Fig.

1. (b) Alignment of the mean EAP-signals from the eight sites along the silicon shank closest to the cell body to the spike initiation time $t_{spike}$ (determined intracellularly) reveals temporal differences between the EAP-signals (left to right). (c) Time difference between the EAP-minimum at different sites along the same shank and the intracellular spike onset (black) or the time of the EAP-negativity of the electrode recording the strongest EAP (cyan). The two shank-sides are considered separately (see Fig. 2a-d, second and third column), hence the multiple lines (x-axis: electrode number as defined in Fig. 2a). (d) Signal-propagation velocity $v$ calculated from the inter-electrode distances (x-axis: electrodes involved in calculation of $v$). AP-minima delays are attributed to somatic action potentials traveling back along the apical dendrites (see text). (e) The same intracellular input as in Fig. 1 delivered to the soma of a L5 pyramidal neuron simulation (see Methods) with extracellular recording sites positioned at the same locations as for the silicon probe (left) and the resulting intra- (top) and extracellular responses (middle and bottom). $V_e$ at a site 30 $\mu$m from the soma is either computed by taking into consideration the entire neuron (middle) or only the soma (bottom). (f) If the same analysis as in panel (b) is carried out for the simulated data, the temporal differences between the EAP-signals along the same shank can be attributed to membrane currents along the whole neural morphology (top). (Notably, the EAP-delay and propagation speed are very similar to the ones measured experimentally for the L5 pyramidal neuron in panels (b) and (c).) An identical simulation with only somatic compartments contributing to the EAP reveals no temporal differences (bottom).

**Figure 4:** Cell type-specific intra- and extracellular spike-waveform characteristics as a function of spike frequency. (a) Intracellular somatic dc current injection of varying strength results in intracellularly (blue) and extracellularly (red) recorded spikes. Spike frequency is defined for each spike as the inverse of its ISI resulting in a Gaussian-like spike frequency histogram (right). (b) Five extracellular spike-waveform characteristics were studied (left to right): the initial capacitive positivity ($V_{e,cap}$) amplitude, the EAP-negativity amplitude ($V_{e,extr}$), the EAP-repolarization positive ($V_{e,repol}$) amplitude, the EAP repolarization time $\tau_e$, and the EAP half-width $\Delta t_{e,hw}$ (features designated in red). Likewise, five intracellular spike-waveform characteristics were analyzed (left to right): change in voltage spike threshold compared to the mean, the intracellular spike-amplitude ($V_{i,extr}$), the intracellular post-spike negativity ($V_{i,repol}$)-amplitude (compared to baseline), the intracellular spike repolarization time $\tau_i$, and the intracellular spike half-width $\Delta t_{i,hw}$ (features designated in blue). (c) Intra- (solid blue) and extracellular (solid red) spike-waveform characteristics as a function of spike frequency for the L5 pyramidal neuron of panel (a). Broken lines indicate the mean of each intra- and extracellular spike-feature across spike frequencies. (d-f) Differences in intra- and extracellular spike waveform characteristics (panel (c)) as a function of spike frequency with reference to the mean waveform across all spikes irrespective of spike frequency for (top to bottom) 8 L23

and 12 L5 pyramidal neuron recordings as well as 4 basket cell recordings (red: extracellullar feature; blue: intracellular features; circles: mean; error bars: std). Differences are expressed as the relative error (for more thorough explanation, see text). $V_{e,extr}$-variability is consistently larger than $V_{i,extr}$-variability for all cell types (second and third column; basket cell variability in the third column, in blue, is attributed to repolarization being very close to baseline) while temporal feature variability much less so (fourth and fifth column).

**Figure 5:** Spike waveform variability with stimulation intensity and spike order. (a) For weak intracellular dc stimulation of a L5 pyramidal neuron (top) the features of the intracellular (blue) and extracellular (red) traces remain largely invariant (broken lines designate AP- and EAP-amplitude of spikes at the beginning and 2.5 s from stimulus onset). For strong stimulation (bottom), intracellular and extracellular traces contain spikes whose amplitude changes with spike order (broken lines; compare with top row). (b) Comparison between 2nd (blue) and 11th intracellular spike (black) aligned at $t_{spike}$ (left) reveals small differences for weak (top) stimulation that become more pronounced for strong stimulation (bottom). (Second from left) Difference between the 2nd and 11th intracellular AP-waveform (mean of five experiments with identical input; blue minus black in leftmost panels). (Third and fourth from left) Same for EAP-waveforms. (c) Intra- and extracellular features as function of spike order (left: $V_{i,extr}$ (blue) *vs.* $V_{e,extr}$-change (red); right: $\Delta t_{i,hw}$- *vs.* $\Delta t_{e,hw}$-change) for weak (top) and strong (bottom) stimulation (same L5 pyramidal neuron as in panels (a-b)). Relative error compared to the last (11th) spike considered (relative error for all features for the 11th spikes equal zero). (d) Slope of the amplitude change (as reported in panel (c); see also text) for the intra- (blue) and extracellular (red) EAPs for L23 (top) and L5 pyramidal neurons (bottom) as a function of stimulation amplitude (circles: mean; error bars: std). Statistical testing (ANOVA, $p$ <0.05) reveals significant difference between the amplitude gradient of intra- and extracellular L5 pyramids. (e) Mean CSD (left shank) of the 2nd and 11th spike for a L5 pyramidal neuron (same as in panels (a-c)) for weak (top) and strong (bottom) stimulation (left two panels). The difference in mean CSD between the 2nd and 11th spike is shown in the rightmost panels. (f) Relative error in amplitude, time and spatial features of the CSD as a function of spike order for a L5 pyramidal neuron as expressed by (left to right) $A_{CSD}/\overline{A}_{CSD} - 1$, $\sigma_t/\overline{\sigma}_t - 1$ and $\sigma_x/\overline{\sigma}_x - 1$ with $\overline{A}_{CSD}$, $\overline{\sigma}_t$, $\overline{\sigma}_x$ being the mean CSD-amplitude, -time and -space constant, respectively (cyan: weak stimulation; black: strong stimulation; two lines: CSD-changes along two sides of the same shank). (g) Slope of the linear fit to the mean $A_{CSD}$ as a function of spike order normalized by the $\overline{A}_{CSD}$ for each cell (blue: intracellular; red: extracellular; circles: mean; error bars: std) for L23 (left) and L5 (right) pyramidal neurons for the four shank-electrodes on the same *vs.* the opposite side of the soma. Statistical testing (ANOVA, $p$ <0.05) revealed no significant difference between intracellular- and

$A_{CSD}$-slopes. Furthermore, no statistically significant difference was found for $A_{CSD}$-slopes between weak and strong stimulation.

**Figure 6:** Comparison between EAP-waveform with the negative first-order time-derivative of the intracellular AP-waveform, -dVi/dt, for different cell types (top to bottom: a L23 pyramid, a L5 pyramid and a basket cell). Intracellular stimuli of varying strength are applied (see Fig. 1) resulting in spikes of varying ISI. Spike frequency is then defined as 1/ISI and spikes are grouped. The figure shows the mean extracellular (red) and the mean -dVi/dt (blue) for difference spike frequencies. (Waveforms are scaled so as to have the same amplitude.) As observed, the EAP- and -dVi/dt waveforms are in close agreement (width, etc.) near the EAP-negativity. Comparison between the EAP- and -dVi/dt waveform becomes poorer approx. 1 ms after the EAP-negativity when slower, repolarizing currents are activated.

**Figure 7:** Impact of EAPs on the local field potential. (a) Spike triggered EAP-waveform of a L5PC (a1, a2) and a L3BC (a3, a4) (left: from site with largest EAP-amplitude; right: from site recording the second largest EAP-waveform). The intact EAP-waveform is shown (red) as well as the 'de-spiked' one where the EAP-negativity is missing (black; window of 0.6 ms around spike initiation time is substituted by a spline). (b) Extracellular traces composed using the L5PC EAP-waveform: mean spike rate $f_0$ of (b1) 1 Hz with intact waveform, (b2) 1 Hz with de-spiked waveform (from panel a2), (b3) 8 Hz and (b4) 30 Hz with intact waveform. (c-e) 50 realizations of a random process (log-normal pdf used to produce the ISI-distributions) to create 9 second traces with $f_0$=1, 8 and 30 Hz, respectively. (f) Mean spectral density as a function of temporal frequency for the intact EAP-waveform shown in panel (a1, red) for different $f_0$ (green: no spiking, red: 1 Hz, black: 8 Hz, blue: 30 Hz). (g) Same as panel (f) for the 'de-spiked' EAP-waveform of the L5PC shown in panel (a1, black). (h) Same analysis as in panel (f) for the intact EAP-waveform of the basket cell shown in panel (a3, red). (i-k) $p$-value ($t$-test) for the pairwise comparison of spectral density at $f_0$=1 (red), 8 (black) and 30 Hz (blue) with no spiking (broken lines: $p$=$10^{-3}$, Bonferroni-corrected) for the cases shown in panels (f-h). (l-n) The same analyses introduced in panels (i-k) but instead of using the EAP-waveform of a single neuron we use EAP-waveforms from all neurons of a particular cell type (8 L23, 4 L4 and 12 L5 pyramidal neurons) to create extracellular voltage traces (as the ones shown in panel b) to emulate MUA with mean spike frequency $f_{MUA}$= 8, 32 and 96 Hz. Statistical significance ($t$-test, dashed line: $p = 10^{-3}$, Bonferroni-corrected) of the difference in spectral power between control (no spiking) and spiking traces at different frequencies for intact (red) and de-spiked (black) EAP-waveforms. Lines of the same color show the result from different EAP-waveforms as measured by different sites along the shank by considering the strongest, second and third strongest EAP-signals both for the intact and de-spiked EAP-waveforms with the lowest $p$-value obtained for strongest EAP-waveforms. For $f_{MUA}$ equal or larger than 32 Hz, intact as

well as de-spiked waveforms of all pyramidal cell types significantly impact spectral density as low as 20 Hz.

Figure 1:

Figure 2:

Figure 3:

Figure 4:

Figure 5:

Figure 6:

Figure 7:

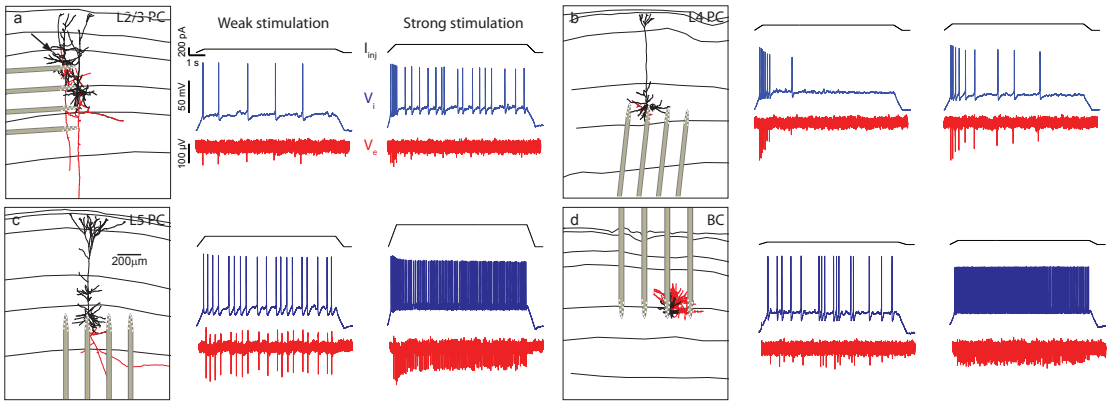
a
L2/3 PC
Weak stimulation
Strong stimulation
200 pA
1 s
50 mV
100 µV
$I_{inj}$
$V_i$
$V_e$
b
L4 PC
c
L5 PC
200µm
d
BC

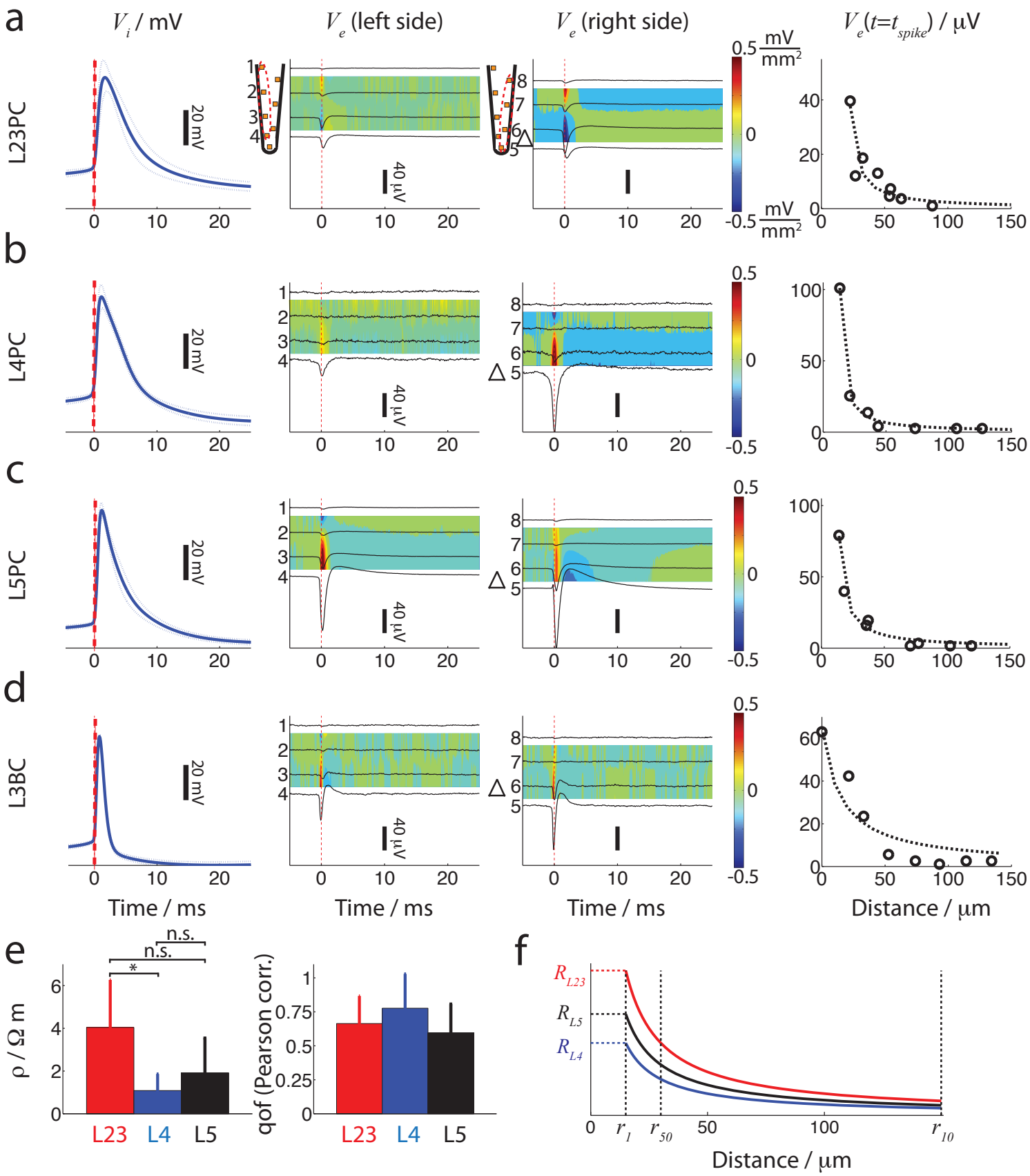
a
b
c
d
e
f
$V_i$ / mV
$V_e$ (left side)
$V_e$ (right side)
$V_e(t=t_{spike})$ / µV
L23PC
L4PC
L5PC
L3BC
20 mV
40 µV
mV/mm²
Time / ms
Distance / µm
ρ / Ω m
qof (Pearson corr.)
n.s.
*
L23
L4
L5
$R_{L23}$
$R_{L5}$
$R_{L4}$
$r_1$
$r_{50}$
$r_{10}$

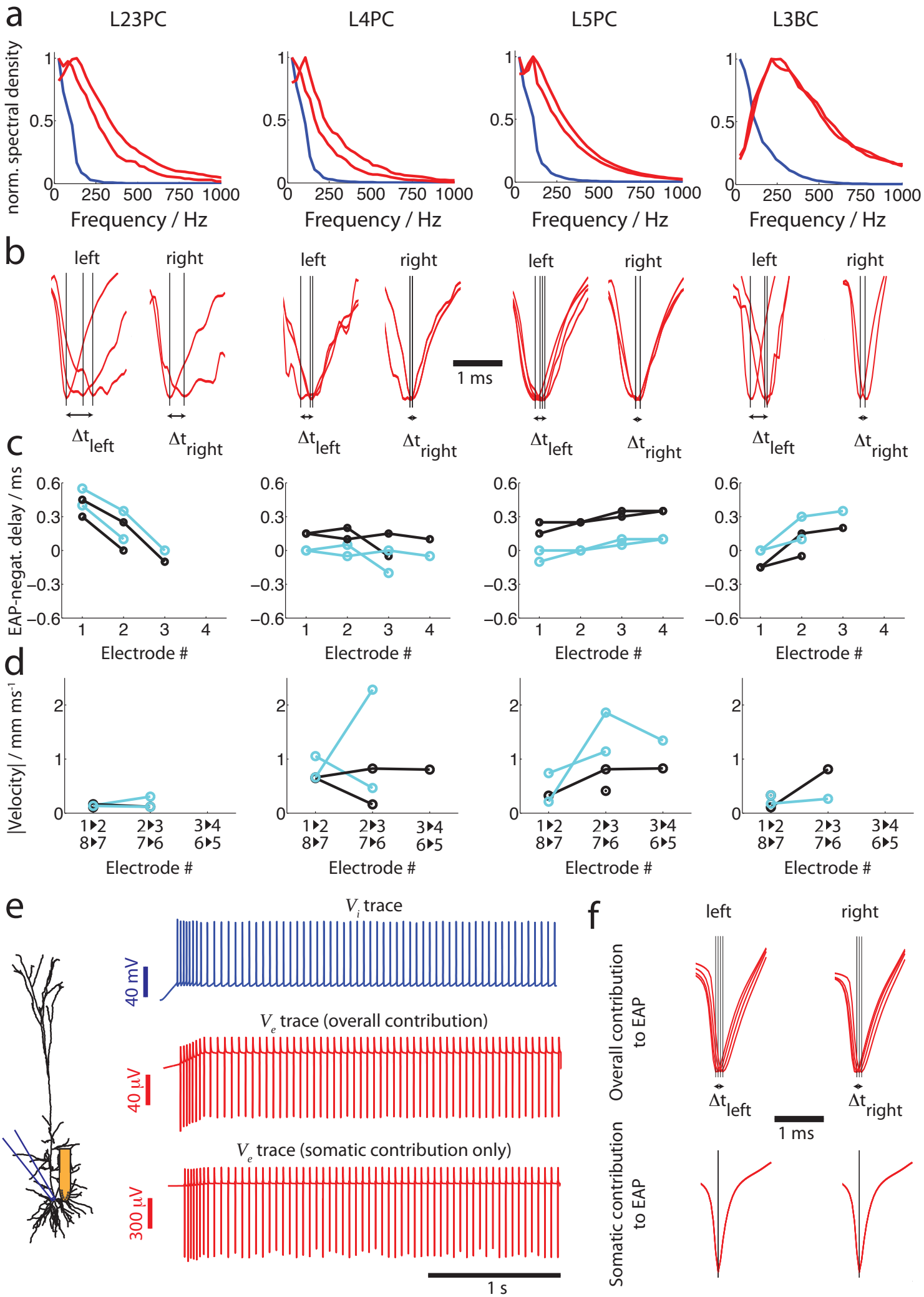
a
L23PC
L4PC
L5PC
L3BC
norm. spectral density
Frequency / Hz
b
left
right
1 ms
Δt left
Δt right
c
EAP-negat. delay / ms
Electrode #
d
|Velocity| / mm ms-1
1▸2 8▸7
2▸3 7▸6
3▸4 6▸5
e
Vi trace
40 mV
Ve trace (overall contribution)
40 µV
Ve trace (somatic contribution only)
300 µV
1 s
f
Overall contribution to EAP
Somatic contribution to EAP

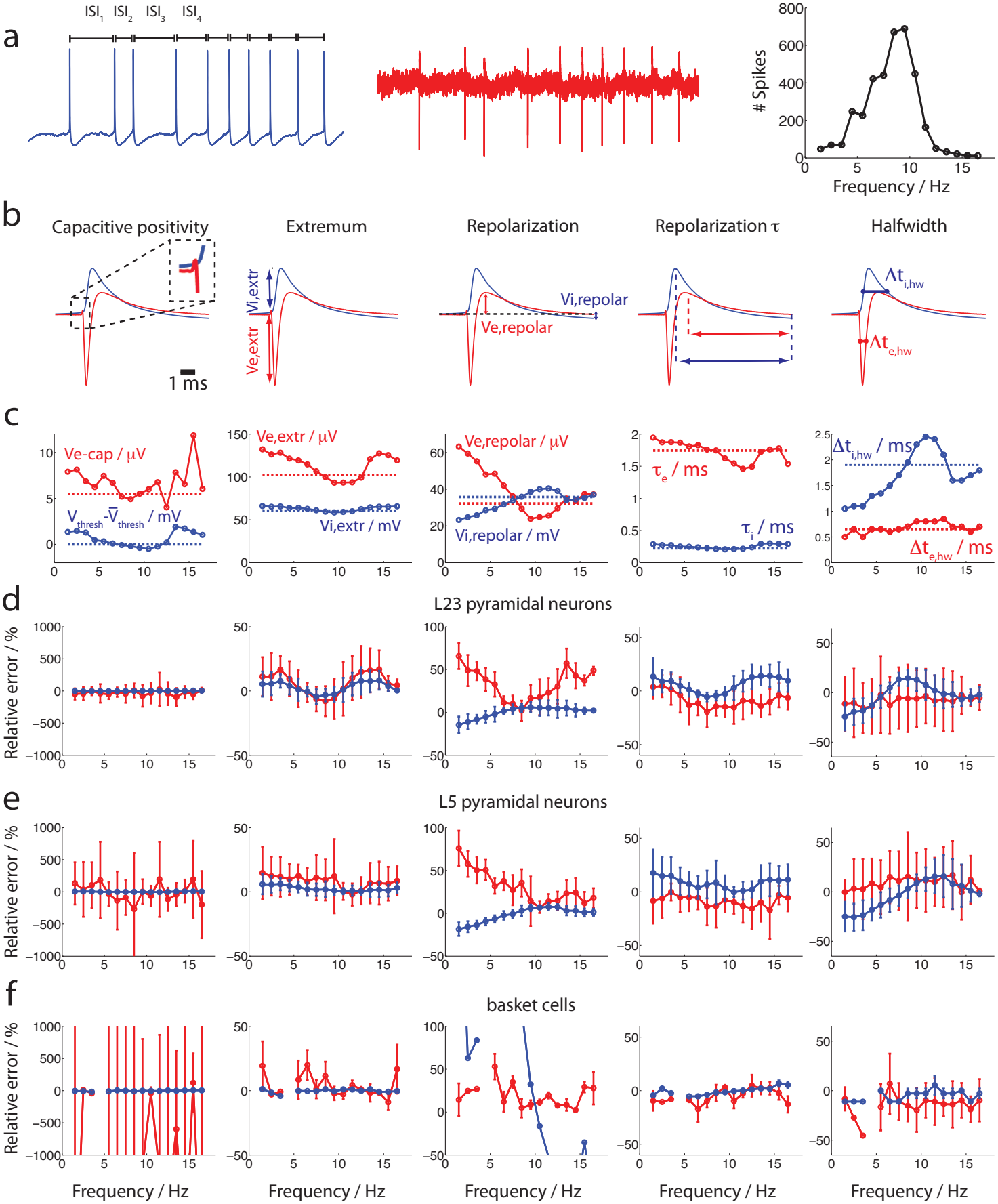
a
ISI1 ISI2 ISI3 ISI4
# Spikes
Frequency / Hz
b
Capacitive positivity
Extremum
Repolarization
Repolarization τ
Halfwidth
1 ms
Vi,extr
Ve,extr
Vi,repolar
Ve,repolar
Δti,hw
Δte,hw
c
Ve-cap / μV
Vthresh-V̄thresh / mV
Ve,extr / μV
Vi,extr / mV
Ve,repolar / μV
Vi,repolar / mV
τe / ms
τi / ms
Δti,hw / ms
Δte,hw / ms
d
L23 pyramidal neurons
Relative error / %
e
L5 pyramidal neurons
Relative error / %
f
basket cells
Relative error / %
Frequency / Hz

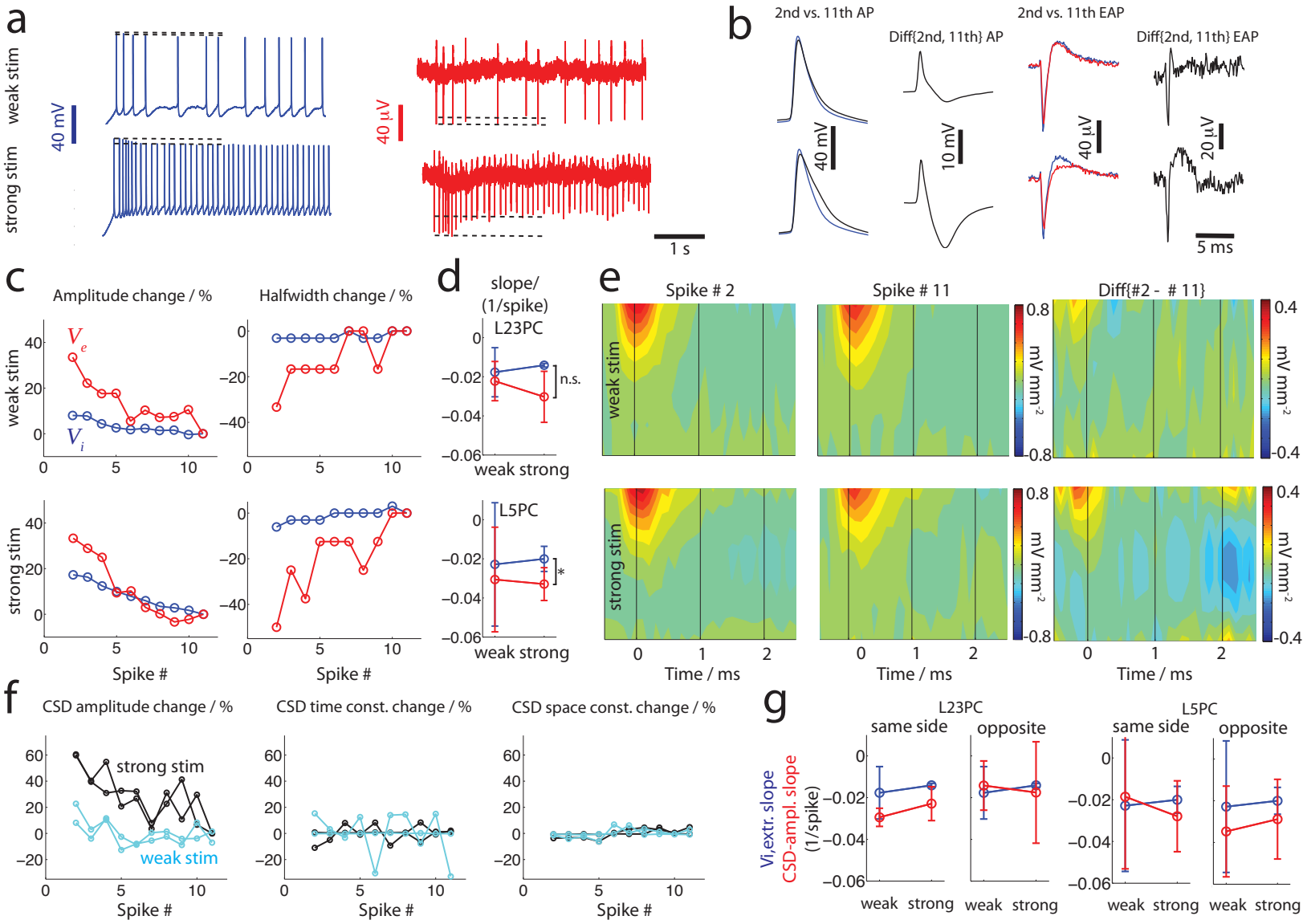
a
weak stim
strong stim
40 mV
40 µV
1 s
b
2nd vs. 11th AP
Diff{2nd, 11th} AP
2nd vs. 11th EAP
Diff{2nd, 11th} EAP
40 mV
10 mV
40 µV
20 µV
5 ms
c
Amplitude change / %
Halfwidth change / %
$V_e$
$V_i$
weak stim
strong stim
Spike #
d
slope/
(1/spike)
L23PC
L5PC
n.s.
*
weak strong
e
Spike # 2
Spike # 11
Diff{#2 - # 11}
weak stim
strong stim
mV mm$^{-2}$
Time / ms
f
CSD amplitude change / %
CSD time const. change / %
CSD space const. change / %
strong stim
weak stim
Spike #
g
L23PC
L5PC
same side
opposite
Vi,extr. slope
CSD-ampl. slope
(1/spike)
weak
strong

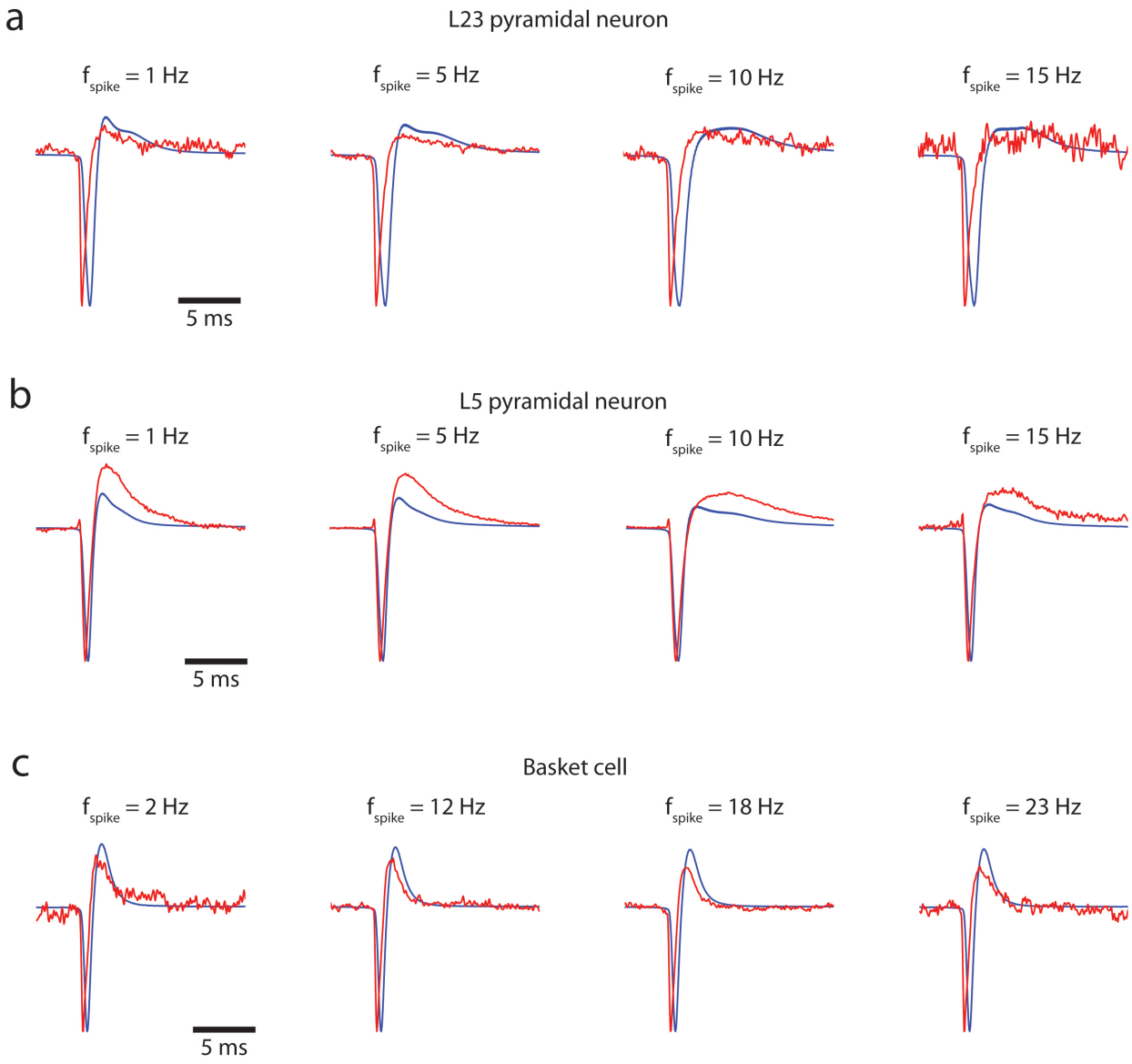
a
L23 pyramidal neuron
f spike = 1 Hz
f spike = 5 Hz
f spike = 10 Hz
f spike = 15 Hz
5 ms
b
L5 pyramidal neuron
f spike = 1 Hz
f spike = 5 Hz
f spike = 10 Hz
f spike = 15 Hz
5 ms
c
Basket cell
f spike = 2 Hz
f spike = 12 Hz
f spike = 18 Hz
f spike = 23 Hz
5 ms

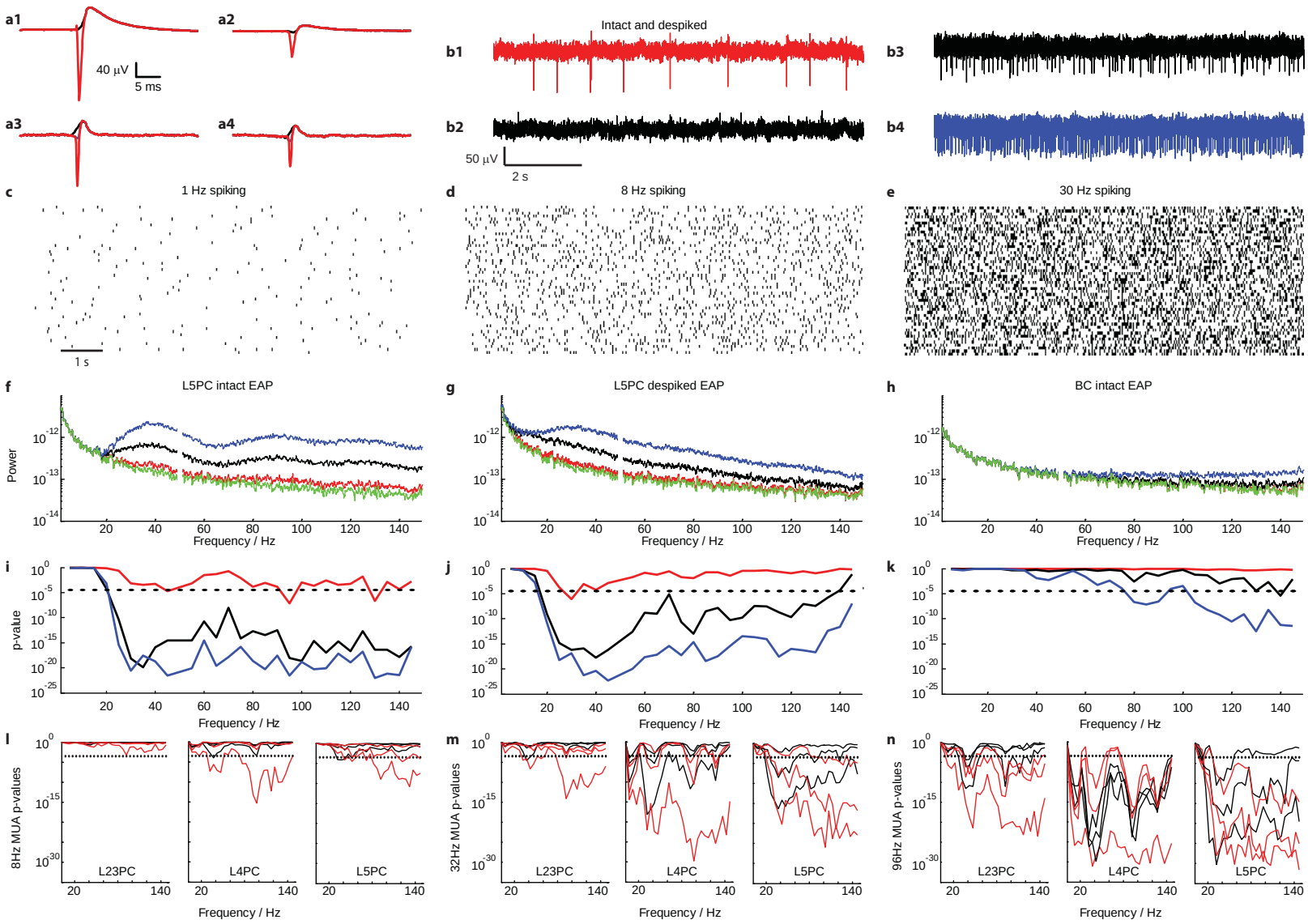
a1
a2
40 µV
5 ms
a3
a4
Intact and despiked
b1
b2
b3
b4
50 µV
2 s
c
1 Hz spiking
1 s
d
8 Hz spiking
e
30 Hz spiking
f
L5PC intact EAP
Power
Frequency / Hz
g
L5PC despiked EAP
h
BC intact EAP
i
p-value
j
k
l
8Hz MUA p-values
L23PC
L4PC
L5PC
m
32Hz MUA p-values
n
96Hz MUA p-values